INL/RPT-22-68606
Revision 0

Mechanics of the Ring Tension Test (RTT): A Finite Element-based Investigation

September 2022

Robert S. Hansen, David W. Kamerman, Philip G. Petersen, and Fabiola Cappia

Idaho National Laboratory

INL is a U.S. Department of Energy National Laboratory operated by Battelle Energy Alliance, LLC

INL/
Revision 0

Mechanics of the Ring Tension Test (RTT): A Finite Element-based Investigation

Robert S. Hansen, David W. Kamerman, Philip G. Petersen, and Fabiola Cappia

September 2022

Idaho National Laboratory
Characterization and Advanced Post-Irradiation Examination
Idaho Falls, Idaho 83415

http://www.inl.gov

Prepared for the
U.S. Department of Energy
Office of Nuclear Energy
Under DOE Idaho Operations Office
Contract DE-AC07-05ID14517

MOTIVATION AND BACKGROUND

Accurate data on the material behavior of anisotropic accident tolerant fuel (ATF) cladding is vital to qualification efforts. Of particular importance are the properties in the hoop (circumferential) direction. However, determination of these hoop direction properties is not straightforward, and it poses significant challenges. Several ring hoop tension test methods have been proposed and implemented in the past; however, they have resulted in significant under- and overestimation of the cladding material strengths. Furthermore, testing of irradiated cladding in a hot cell environment introduces additional experimental uncertainties, making robust testing even more challenging. Clearly, there is a critical need for a thorough review of the uncertainties associated with experimental testing in addition to improvement and optimization of hoop tension testing methods. This work addresses this need through extensive investigation of ring tension testing methods via finite element analysis. The manuscript contains a comprehensive review of the state of the art, a comparison of leading test method candidates, a parameter sensitivity study, and ultimately a mechanics-based approach to extracting the critical strength measurements. It concludes with recommendations for the most robust experimental method and data processing path to be used in future testing of ATF cladding and other potential materials to be used in nuclear reactors with challenging thin wall tubing type geometry.

Page intentionally left blank

ABSTRACT

The ring tension test (RTT) is an experimental method for determining mechanical behavior in a material's circumferential or hoop direction. It is a crucial test for testing anisotropic materials with tube geometry, such as nuclear fuel cladding or irradiated pipes. Several RTT configurations exist, each with their own advantages and disadvantages. However, this test is significantly more complex than traditional tensile testing and can be especially sensitive to small differences and inconsistencies in the test setup and geometry, ultimately affecting the derived mechanical properties. Previous research has focused on method development, and little work has been done on understanding the subtle differences between an ideal test and experiments, specifically when the tests are performed on highly irradiated materials in hot cells. In this work, a finite element-based investigation of the RTT is conducted. Two promising test configurations are investigated, comparing their ability to determine accurate material strengths through plastic deformation. Several non-ideal conditions and uncontrollable effects which are likely to occur during experimental testing such as machining tolerances, variations of specimen geometry from nominal dimensions, rotation of specimens and fixturing, and other test setup discrepancies are studied. The sensitivity of measured strengths to these conditions is presented. A mechanics-based approach to describing and correcting raw data to determine actual strengths is also included for one of the configurations, resulting in a robust correction method with highly accurate material strength measurements. Based on these analyses, the hemicylindrical mandrel configuration is recommended with a gauge region oriented at a 45° angle.

CONTENTS

FIGURES

TABLES

Page intentionally left blank

ACRONYMS

ASTM	American Society for Testing and Materials
ATF	Accident tolerant fuel
BNL	Brookhaven National Laboratory
DOE	U.S. Department of Energy
FE	Finite element
ID	Inner diameter
LOCA	Loss-of-coolant accident
NFCSC	Nuclear Fuel Cycle and Supply Chain
OD	Outer diameter
PEEQ	Equivalent plastic strain
PNNL	Pacific Northwest National Laboratory
PTFE	Polytetrafluoroethylene
PWR	Pressurized water reactor
RIA	Reactivity-initiated accident
RTT	Ring Tension Test
UE	Uniform elongation
UTS	Ultimate tensile strength
UV	Ultraviolet
VM	Von Mises
YS	Yield strength

Page intentionally left blank

Mechanics of the Ring Tension Test (RTT): A Finite Element-based Investigation

1. INTRODUCTION

The Ring Tension Test (RTT) is one of the possible mechanical testing methods for determining hoop direction properties in materials with thin-walled tubular geometries. For materials with texture and mechanical anisotropy, such as zirconium alloys used in fuel cladding [1] and additively manufactured tubes [2], plastic behavior varies with the testing direction. As a result, determination of yield strength (YS), ultimate tensile strength (UTS), and uniform elongation (UE) requires the tests to be direction specific. Accurate evaluation of tensile hoop properties is essential for fuel cladding, as the highest stresses are generated in the hoop direction during in-reactor operation [3]. Appropriate test method selection and test parameter uncertainty evaluation is therefore essential in evaluating tube tensile hoop properties.

While other hoop direction tests exist, each with their own advantages and drawbacks [4], the RTT is the focus of this work. One of the earliest uses of a RTT was by Price in 1972, who used hemicylindrical mandrels (also called D-shaped mandrels, or split-disks) which fit inside the ring [5]. The mandrels are then pulled apart by a universal testing machine, in turn pulling the ring in tension in the hoop direction. It generally produces a nearly uniaxial stress state, although some variations have been designed to induce stress biaxiality [4]. A major benefit of the RTT is that it requires relatively little material per test compared to other tests like a burst test. The reduction of needed material is ideal when the available material for testing is limited, expensive or difficult to handle, such as in the case of irradiated cladding. Test configuration variations include different specimen geometry as well as design of different grips and fixtures or specimen position during the test. All these factors can contribute to test outcome differences.

Regarding the specimen geometry, some rings have no gauge region [6], [7], others feature only one gauge, [5], [8], while others utilize two gauge regions located on opposite sides of the ring [9]. The dimensions of the gauges also vary, with gauge length-to-width ratios of approximately 1:1 [10], [11], 1.5:1 [12], 2:1 [13], and 4:1 [8], [14], [15]. In some cases, shorter gauges have been found to cause early onset of necking, with failure occurring at stress-concentrating fillets at the end of the gauge, indicating that longer gauges perform better [16]. The ASTM Standard E8/E8M-21 also recommends longer gauges, with a length-to-width ratio of roughly 4:1 [17], although this requirement applies strictly to traditional axial tension testing of metallic materials and might not be fully applicable to the RTT configuration. Longer gauges also tend towards more uniaxial stress, while shorter gauges can result in stress biaxiality, as fillet regions at the end of the gauge have a greater impact on the stress state in the entire gauge [4]. It is worth noting that in some cases, stress biaxiality is desired in ring tests, such as in replicating accident conditions. For these cases, plane-strain specimens have been developed which use narrow notches in a wider ring to induce the appropriate stress biaxiality [18]. These plane-strain tests show through-thickness slip resulting in failure [19], while uniaxial loading generally causes failure by through-width slip [14].

Another key difference between RTT variations is their ability to maintain spatial uniformity of both stress and strain during testing, within the region of interest for the particular specimen (e.g., the gauge region). Non-uniformity can cause early failure, inaccurate determination of material properties, and it can over- or under-emphasize the effect of defects. Although uniformity may seem like a straightforward goal, it can be impacted by a variety of factors. For instance, when the mandrel radius is much smaller than the inner radius of the ring being tested [20], as seen in Figure 1(a), significant bending occurs in the ring at the gap between the mandrels as the ring is straightened into an oval shape. Some researchers have used a finite element (FE)-informed approach to attempt corrections to account for the extreme bending, using data from traditional tensile tests and isotropic materials [21]. More recently, empirical relationships derived from finite element models have been proposed to relate load-displacement curves from this small mandrel configuration to yield strengths, for a range of materials and test geometries [22]. The lack of a gauge in this method may be beneficial for applications like testing irradiated materials, where machining a gauge region in a hot cell may be challenging or not possible. However, the severe bending and the lack of gauge region make it challenging to extract desired measurements and material properties. Even in cases where the mandrel and ring inner radius match more closely, undesirable bending occurs in the ring at the gap between the mandrels [23]. This results in non-uniform deformation at that location, as the inner face of the ring is placed in tension while the outer face is placed in compression [24]. Nevertheless, researchers have used rings with the gauge placed at this gap (Figure 1(b)), correcting for the bending challenges with a finite element model-informed inverse method to determine stress-strain behavior [25], [26].

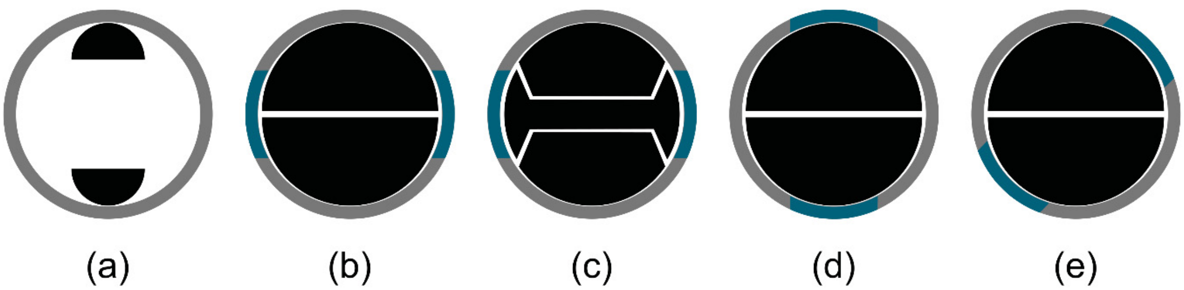

Figure 1. Comparison of various RTT arrangements. The ring is shown in gray, with blue regions marking the gauge. Grips (both mandrels and a dogbone insert) are shown in black.

To counteract this bending moment, Arsene and Bai recommended an evolution of the Figure 1(b) with a "dogbone" insert placed in between the mandrels, supporting the ring across the length of the gauge region and preventing inward bending, as seen in in Figure 1(c) [23]. Other studies followed this recommendation, using the "dogbone" method for a variety of length-to-width ratios of the gauge [14], [27]. However, drawbacks exists for this method too; although it mitigates the bending with the dogbone insert, it creates non-uniform strains in the gauge, with peaks at either end of the dogbone [16]. Instead of using a dogbone insert to prevent bending, other researchers have proposed rotating the gauge so that it is supported by the hemicylindrical mandrel, either being located at the top of the mandrel [15], [28], as in in Figure 1(d), or rotated between the top and the side, often at a 45° angle [8], [29], as in in Figure 1(e). Both of these configurations have the advantage of preventing bending while maintaining the same curvature throughout the test, but the results are more heavily affected by the increased friction, which can be a significant shortcoming for this test configuration. In this regard, the 45° angle configuration tends to have a lower impact from friction, striking the balance between friction and bending.

Friction between the ring and mandrels/insert has an established effect on the stress state of the ring, with small changes in friction coefficients having significant impacts on deformation uniformity [30]. The presence of friction along the mandrel-to-ring interface also results in a lower load carried by the ring compared to the load applied by the test frame; this means that the apparent stress (calculated with the load frame force) is higher than the actual stress experienced by the ring [8]. This discrepancy is minimized as the friction is reduced, meaning that lower friction coefficients and shorter interface lengths (like those offered by the dogbone method, Figure 1(c)) offer better load agreement. This has led some researchers to use the small mandrel configuration in Figure 1(a), where the relatively short interface between the ring and mandrels greatly reduces the effect of friction [21], [22]. Researchers who implement the other test configurations have taken precautions to reduce friction as much as possible, regardless of the RTT method chosen. PTFE (Teflon) tape or sheet has been used on the mandrels, sometimes paired with vacuum grease, in order to reduce the coefficient of friction between the mandrels and ring [29]. The use of PTFE tape allowed reduction of the friction coefficient to values of 0.02-0.04 compared to 0.3 for the non-lubricated case [16], [18]. However, the tape can only be used for temperatures up to ≈260°C [31]. Graphite-based lubricants have also been used, which allow much higher temperatures than the Teflon tape, although they have a higher coefficient of friction than the tape [12], [28]. A Tungsten disulfide coating on mandrels has also been used for this same purpose [14]. Instead of using lubrication, novel mandrel designs, which use a series of rollers on the mandrel surface to reduce mandrel-to-ring friction, have also been investigated [32]. Application of this design has been limited to samples with diameter >50mm and it is likely that application to much smaller tubes of interest in this work is not feasible.

Some researchers have posited that the tensile load in the ring varies, and is a function of both the friction and the angle of gauge orientation, choosing a 45-degree orientation rather than a top arrangement (Figure 1(e) vs Figure 1(d)) [8], [13]. Where friction can be significantly reduced through PTFE tape and/or vacuum grease, researchers have noted little difference in measured strengths when placing the gauge at different angles [13], although there were some differences in distribution of strains in the gauge [33]. However, friction is still expected to be a significant factor in cases where lubricant use is limited (such as high temperatures or for remote testing of irradiated materials) and so gauge orientation angle may still be an important factor affecting measured YS and UTS to be investigated. Current state of the art focuses very little on the uncertainty caused in higher friction cases, except for noting that friction should be minimized and treating as if it is negligible. A methodology for correcting load and stress measurements, based on these angles and friction, would be especially beneficial for accurate determination of material properties in the instances where friction is not negligible.

Another source of test result variation is the relative geometry between specimen and fixturing grips. While gaps and clearances between the mandrels and the ring have been noted for their potential impact to test results, they have not necessarily been thoroughly studied. For the dogbone method, Arsene and Bai noted the need for optimizing the clearances between the ring and fixturing. They observed that a large gap between the ring and the mandrel at the top/bottom causes premature loss of contact with the dogbone insert, while a small gap will increase bending in the wider (non-gauge) part of the ring [23]. They proposed a force correction factor as a function of displacement, noting that it likely depended on test geometry [12]. Martin-Rengel proposed using the same force correction factor based on the fixture-ring gap, but noted that in addition to being displacement- and geometry-dependent, it was also material-dependent except for at small displacements [10]. Nagase observed that the clearance between the mandrels and the ring causes a gradual curve or "ramp-up" in the load-displacement curve before developing linear elasticity [16]. Nindiyasari investigated the effect of a few different mandrel radii, evaluated the location of maximum stress and recommended a mandrel radius equal to the inner radius of the ring [15]. However, a gap must exist to allow placement of the ring on the mandrel, keeping the optimal case unpractical to achieve. Bae investigated the effect of fixturing-ring clearances on the load-displacement curve, noting that larger clearances caused greater distortions in the curve, although no quantification of the effect on measured properties like YS and UTS was performed [34]. The body of work to this point suggests that clearances and gaps in the fixturing are sensitivities that impact the test results.

As described above, even small variations in the RTT geometry cause differences in measured material properties such as YS and UTS. Quantifying the influence of those parameters is of particular importance, especially since clearances are determined by several factors. In addition to variation in the machining tolerance of fixturing, the geometry of the fabricated rings can also vary, sometimes uncontrollably. In the case of irradiated nuclear fuel cladding, the diameter of the cladding changes in reactor due to thermal and irradiation-induced creep [35] or due to fuel swelling once the gap closes [36], [37]. The extent of diametral change, in turn, can vary depending on several factors, such as the specific zirconium alloy [38], neutron flux, irradiation history, and extent of oxidation [39]. Moreover, the diameter of the cladding can vary between different axial locations within the same parent rod due to local differences in the aforementioned irradiation conditions [40]. As a result, the inner diameter of irradiated cladding rings being tested can be difficult to predict, and actual fixturing-ring clearances may be significantly different than those expected based on the as-fabricated ring dimension and nominal fixturing design. This inherent uncertainty and variability of test geometry illustrates the need for better understanding of the effect that these uncontrollable variations related to experimental uncertainties might have on RTT results.

While RTTs have been used extensively, this review of the state of the art demonstrates that the specifics have varied widely in terms of specimen geometries, fixture designs, clearances and force corrections. While past research has indicated that varying some of these parameters could influence test results, the relative importance of each parameter compared to the others has rarely been evaluated. Understanding the mechanics of the RTT test and the impact of these various modifiable parameters is needed and vital for robust comparison of results from different test implementations, and for accurate determination of material properties.

This paper addresses this need, using a finite element-based approach to modeling the RTT. Two main subdivisions of the RTT are investigated: the central insert (or "dogbone") method seen in Figure 1(c), and the hemicylindrical mandrel (or "hemi") method in Figure 1(e), each using a ring with a reduced-width gauge section. While each of the configurations addressed in this section have their merits, the hemi and dogbone configurations represent the evolution from earlier concepts and have been the focus of much of the work already in the literature. They also show great promise for measurement of material properties, and thus benefit the most from this evaluation. First, the uniformity of stress and strain in the gauge are considered. Then, a comprehensive investigation of possible geometry effects is given. A study of the correction factors needed to produce accurate strength measurements from experimental load-displacement curves is then presented. A novel mechanics-based explanation for the tensile load carried by the ring in the hemi method is also included. Finally, the two methods are compared, and the important test geometry parameters to monitor are suggested.

2. METHODS

The investigation of the dogbone and hemicylindrical ring tension tests was performed using finite element modeling in Abaqus standard, using implicit analysis. For this work, a base model of both the dogbone and hemi methods was generated, simulating the conditions of an experimental RTT setup as seen in Figure 2. In each case, the ring was modeled with linear 8-node reduced integration (C3D8R) elements to allow for accurate modeling of contact while preventing shear locking. The mandrels and dogbone insert were modeled with analytical rigid surfaces; as fixturing is designed to be much stiffer than the deforming ring with its reduced gauge cross section, this rigid assumption is valid and improves computation time. Mesh refinement was performed using mandrel load at UTS as the convergence metric, resulting in a mesh density of roughly 10 elements/mm through the gauge region, with at least five elements through the wall thickness (the smallest geometry dimension). This number of elements in the gauge thickness is consistent with or higher than previous studies [8], [16]. Where practical, symmetry boundary conditions were used to reduce the computational cost, resulting in quarter geometry from the dogbone model and half geometry for the hemi model.

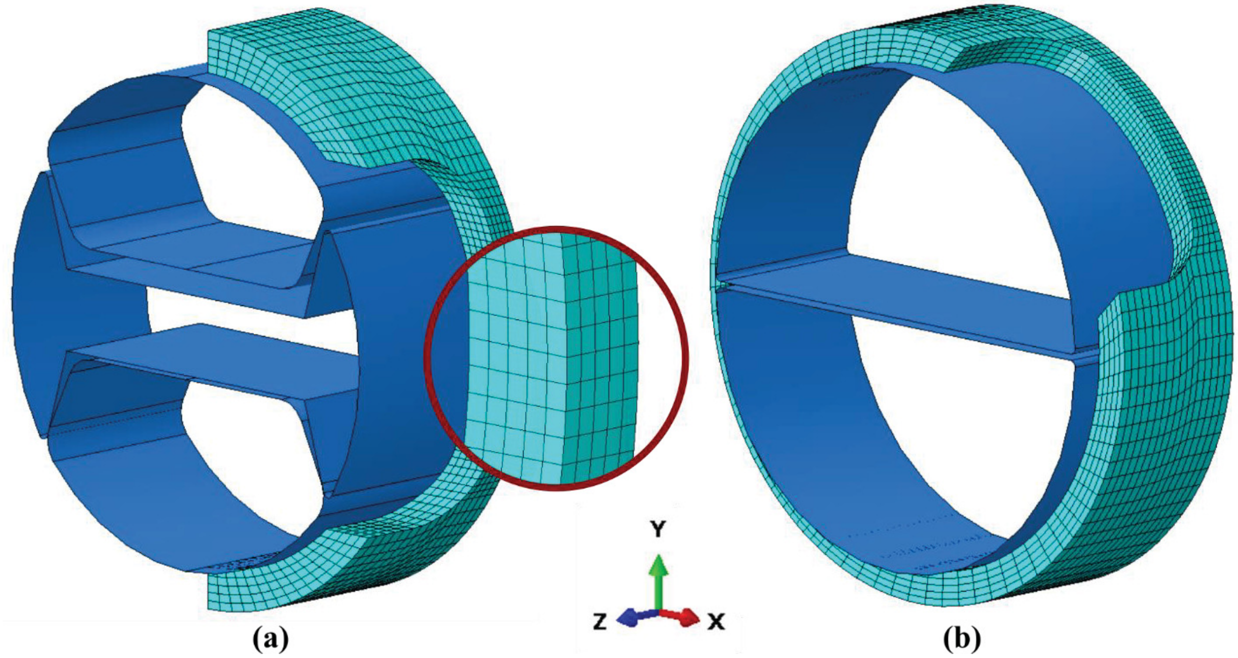

Figure 2. Abaqus models showing meshed ring specimens and rigid fixturing for (a) the dogbone method, featuring quarter symmetry, and (b) the hemicylindrical method, featuring half symmetry.

The geometry of the dogbone setup was based on an existing design [41], with the ring specimen featuring a reduced gauge region with a 4:1 length-to-width ratio. The hemi setup used nearly identical ring dimensions, with the only changes being slightly different ring diameters, a slightly shorter gauge at a 3:1 length-to-width ratio, and the use of only one gauge. Since angle-dependent friction is more significant for the hemi, as described in the introduction, the shorter gauge was chosen to improve the stress distribution. The base dimensions of the ring, gauge, and fixturing are given in Table 1, and their definition can be found on the diagram in Figure 3.

Table 1. RTT dogbone and hemi geometry dimensions.

	Dogbone	Hemi
Number of gauges	2	1
Ring outer diameter (OD), mm	9.39	9.50
Ring inner diameter (ID), mm	8.03	8.36
Ring wall thickness (TH), mm	0.68	0.57
Ring width (RW), mm	5.00	5.00
Gauge length (GL), mm	4.00	3.00
Gauge width (GW), mm	1.00	1.00
Gauge radius (GR), mm	1.00	1.00
Mandrel diameter (MD), mm	7.96	8.24
Mandrel fillet radius (MF), mm	0.50	0.10
Dogbone diameter (DD), mm	7.82	N/A
Dogbone fillet radius (DF), mm	0.10	N/A
Dogbone design angle (DA), °	33.6	N/A

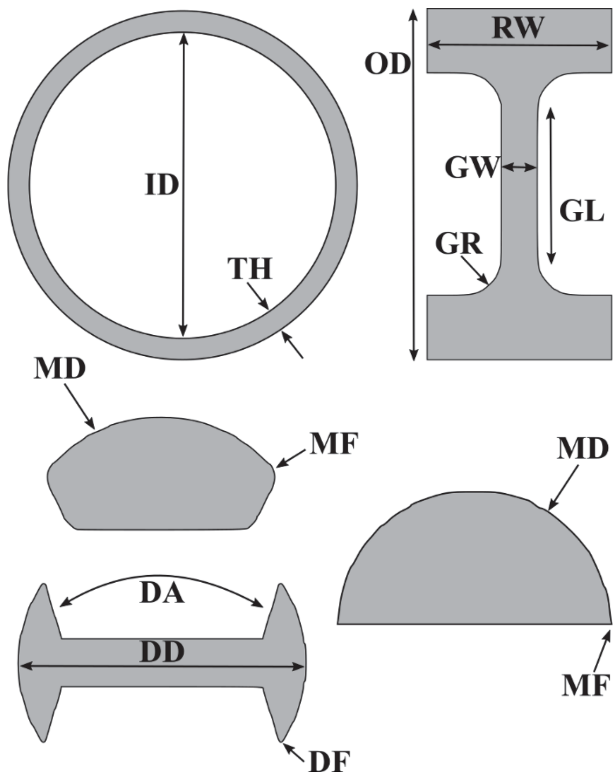

Figure 3. Schematic showing the ring geometry (top left and right), dogbone fixture geometry (bottom left), and hemi fixture geometry (bottom right). Corresponding dimensions are given in Table 1.

The model implemented frictional contact, with a coefficient of friction of 0.1 to simulate a lubricated fixturing-ring interface. This is similar to the state of friction used by previous researchers [8], [10], [12]. The material modeled was unirradiated Zircaloy-4, with plasticity behavior defined by the strength coefficient and strain hardening exponent of a moderately cold-worked metal, calculated using correlations from a Pacific Northwest National Laboratory technical report [42]. The nominal 0.2% offset YS, UTS, and UE of the modeled material are 626 MPa, 846 MPa, and 0.1507, respectively.

The FE model mimicked an experimental setup under displacement control, with the upper mandrel being translated in the vertical direction (y-direction in Figure 2) in specified increments, while the lower mandrel was constrained. The applied top mandrel displacement was used for the raw displacement data that would be measured experimentally, and the reaction force of the top mandrel was the load that would be measured by the load cell experimentally. In the case of the dogbone method, the dogbone insert was unconstrained in the y-direction other than a small constant force in the negative y-direction to simulate a gravity load. This load was set to one newton, which was a sufficiently high load to ensure the correct starting position and facilitate model convergence while remaining insignificant compared to the forces that determine insert movement during the test (i.e. the frictional and normal forces exerted by the ring on the insert). Previous studies often ignore potential dogbone insert motion, assuming that the dogbone stays centered in the center of the ring either through constraints or planes of symmetry [4], [10], [23], [34]. However, in practice there is no such physical constraint to the dogbone; during an experiment it would be free to move up or down inside the ring during the duration of the test. Initial simulations with the gravity load showed that the dogbone did not remain at the ring centroid, but started at a lower position and moved vertically relative to the centroid of the ring. As the gaps and clearances between the ring and fixturing are key parameters under evaluation, and as the position of the insert directly impacts those gaps, the model was built to allow the realistic insert movement typical of experimental conditions.

For each simulated test, displacement was applied past the UTS, ensuring that necking and load reduction had occurred. However, it is worth noting that the data past this point of UTS is not necessarily accurate and thus the load-displacement curve is only qualitative, as ring failure was not simulated, and damage accumulation was not incorporated into the model. For the initial comparison between the dogbone and hemi, the strain and stress distribution were monitored, as well as the resulting load-displacement curves. For the geometry and shape effects investigation, one single parameter was varied at a time. The test matrix of varied parameters is given by Table 2. Degrees are measured counterclockwise from the right side (3 o'clock position), as shown in Figure 4.

The ring inner diameter increments were chosen based on the gap between the ring and the central insert (dogbone) or the mandrel (hemi), resulting in a gap that was 0.25x, 0.50x, 0.75x, 1.5x and 2.0x the original. For the dogbone, a 0.14x gap was also chosen to most closely replicate the gap used in the original dogbone design by Arsene and Bai [23]. In studying the gauge width mismatch for the dogbone, the average gauge width was maintained, meaning the width of one gauge in the model increased and the other decreased. As a note, the dogbone model was based on the design of [41], which allowed some rotation of the dogbone insert between the mandrels (1.1°) at the test initiation boundary condition. The rotation of the ring was constrained by features on the dogbone insert in this same design, only allowing a slight rotation (up to 3.75°) of the ring relative to the dogbone insert. Thus, the rotation of the insert, the ring, and the combined effect were studied for the dogbone method. Eccentricity was caused by an offset of 0.1mm of the ring inner and outer diameter, resulting in a thinner portion of the ring, opposite to a thicker portion. Ovality was caused by elongating the ring, resulting in a major axis 0.1mm greater than the nominal diameter, and a minor axis 0.1mm less than nominal. Original ring rotation is given by the angle of the midgauge, rotation of the eccentric ring is given by the angle location of the thinner part, and rotation of the oval ring is given by the angle location of the major axis.

Table 2. Test matrix for geometry and shape effects analysis.

Parameter	Dogbone	Hemi
Ring inner diameter	8.03mm + 0.1, 0.2 (1.5x, 2.0x gap) - 0.05, 0.1, 0.15, 0.18 (0.75x, 0.50x, 0.25x, 0.14x gap)	8.36mm + 0.06, 0.12 (1.5x 2.0x gap) - 0.03, 0.06, 0.09 (0.75x, 0.50x, 0.25x gap)
Ring wall thickness	0.68mm ± 0.05	0.57mm ± 0.05
Ring width	5.00mm ± 0.2	5.00mm ± 0.2
Gauge length	4.00mm + 0.20 - 0.25, 0.50, 0.75, 1.00	3.00mm + 0.25, 0.50, 0.75, 1.00 - 0.25
Gauge width	1.00mm ± 0.1	1.00mm - 0.25
Gauge width mismatch	0.1mm, 0.2mm, 0.3mm	N/A
Mandrel diameter	7.96mm ± 0.1	N/A
Dogbone diameter	7.82mm ± 0.1	N/A
Dogbone fillet radius	0.10mm + 0.1 - 0.05	N/A
Dogbone design angle	33.6° + 1.6°, 6.4° - 1.6°	N/A
Dogbone rotation	+ 1.1°	N/A

Parameter	Dogbone	Hemi
Ring Rotation	0° + 3.75°, 4.85° (ring, ring + dogbone)	45° ± 5°, 15°, 30°
Eccentricity	Thinnest angle: 0°, 90°, 270°	Thinnest location: 0°, 45°, 90°, 135°, 180°, 225°
Ovality	Major axis angle: 0°, 90°	Major axis angle: 45°, 135°
Friction, μ	0.1 ± 0.05, 0.10	0.1 ± 0.05, 0.10

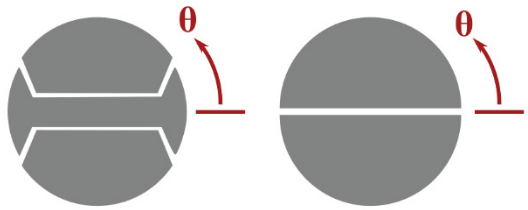

Figure 4. Schematic showing angle convention used in dimensions and parameter identification.

3. RESULTS

3.1 Ideal Geometry Investigation

The first investigation of tests used the geometry and setup parameters given in Table 1, directly comparing the two setups. Figure 5 shows the raw normalized load vs apparent strain curves for both the dogbone and hemi. The load (reaction force of the upper mandrel in the FE analysis) is normalized by the cross-sectional area of the gauge, and is divided in half for the hemi to account for the difference in symmetry modeling between the hemi and dogbone. Apparent strain is calculated as an engineering strain, dividing the deformation by the nominal arc length of the gauge region. These calculations allow a more direct comparison between the slightly different geometries.

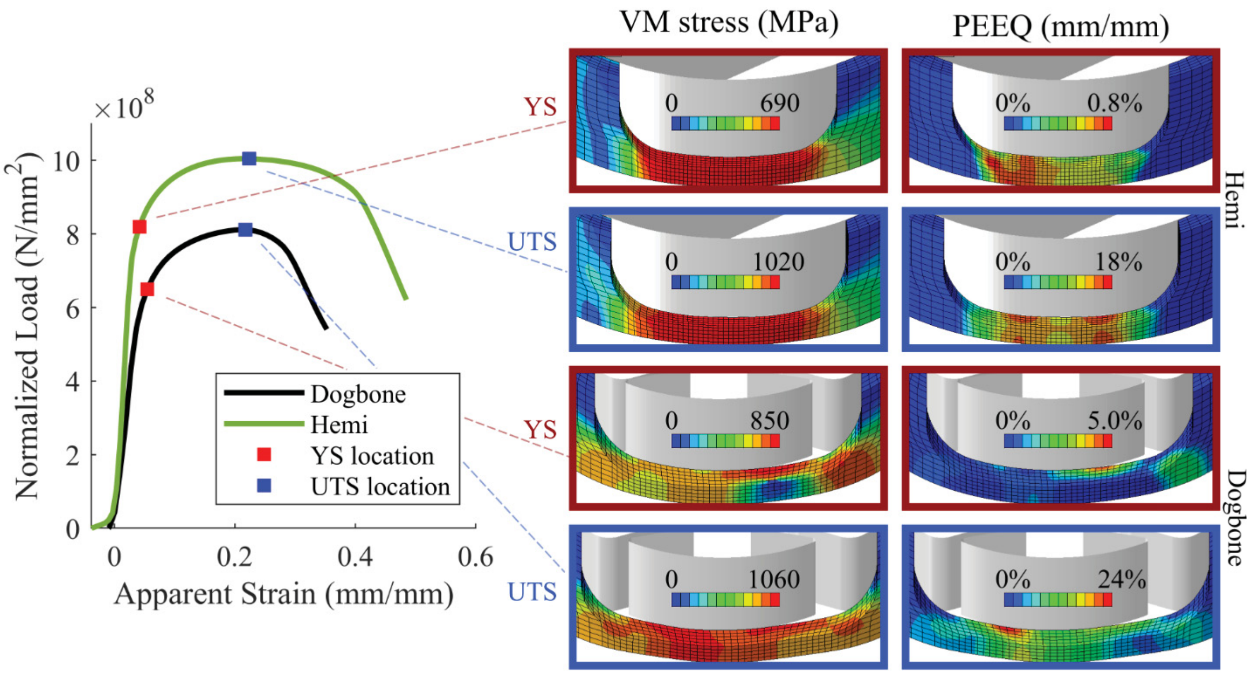

Figure 5. Comparison of dogbone and hemi RTT methods. On the left, plot of normalized load vs apparent strain. On the right, FE contours at the step just after calculated 0.2% offset YS, outlined in red, and at greatest load (UTS), outlined in blue. Load is normalized by cross-sectional area of gauge. The stress contours in left column show von Mises stress (VM), and the plastic strain contours in right column show equivalent plastic strain (PEEQ). In each contour, the mandrel to the right is the mandrel being moved to impose displacement.

Table 3: Mean and standard deviations of the VM stress and PEEQ in the reduced gauge region at the increments of YS and UTS as shown in Figure 5.

			VM Stress (MPa)	PEEQ (mm/mm)
Hemi	YS	Mean	674	0.56%
		Standard Deviation	9	0.09%
	UTS	Mean	984	14.18%
		Standard Deviation	21	1.98%
Dogbone	YS	Mean	654	0.97%
		Standard Deviation	148	1.06%
	UTS	Mean	954	12.01%
		Standard Deviation	53	4.38%

Figure 5 also shows the degree of uniformity of VM stress (left column) and equivalent plastic strain (right column), for both tests at notable points in the test: at the analysis increment just after the 0.2% offset yield point (contours outlined in red, labeled YS), and at the increment of maximum load (contours outlined in blue, labeled UTS). The accompanying Table 3 gives the mean value and standard deviation of the stress and plastic strain for the elements in the gauge region, illustrating the uniformity of each test. These contours show a clear difference between the behavior of the dogbone and hemi setups. The stress contour of the hemi at YS is very consistent with the UTS contour, while the dogbone stress contours at YS and UTS are more distinct. This suggests greater stability of the loading conditions through the duration of the test for the hemi compared with the dogbone. For the hemi test, the stresses are very uniform throughout the gauge at both increments, as seen by the small standard deviation at both YS and UTS in Table 3. For the dogbone, the stresses are not nearly as uniform, with a standard deviation of elements in the gauge at YS roughly fifteen times higher than for the hemi This non-uniformity is explained by the stress concentration near one end of the gauge, consistent with a bending moment. This gauge location is unsupported by fixturing, as it is located at the gap between the dogbone insert and the mandrel. While stress uniformity has improved by UTS, it does not approach the uniformity of the hemi setup. Based on these stress contours, the hemi method produces a stress state much closer to a traditional uniaxial test than the dogbone method does. It is worth noting that while the normalized load at UTS is much higher for the hemi than for the dogbone, the max stress in the contour (which is true stress by nature of the FE analysis) is very comparable between the two methods. This indicates that there is some discrepancy between the load exerted by the mandrel and the stress experienced by the gauge in one or both methods.

All four plastic strain contours are visibly less uniform than the stress contours as expected. However, the plastic strain appears to be more uniform in the hemi than in the dogbone arrangement. This is evident by comparing the standard deviations for the strains reported in Table 3; as with the stresses, the hemi test produced a much more uniform distribution of strains within the gauge region. Comparing the plastic strains at the representative yield point, the simulation results show a peak strain of roughly 5% at the location of the stress concentration for the dogbone, much higher than the 0.8% of the hemi. As the point was chosen just after the 0.2% offset estimate of YS from the normalized load-strain curve, a plastic strain just over 0.2% is expected for an ideal test. This indicates that the dogbone is likely producing premature yielding, as some locations experience plastic deformation much earlier than the rest of the gauge region. The distribution of strain along the gauge for the hemi is noteworthy; rather than a midgauge location for peak strain, the ring shows peak strains located symmetrically on either side of the midgauge. Unlike the concentrations of the dogbone, this location of the peak strain is fully supported by the mandrel, making it unlikely that a bending moment is the cause. Rather, this type of distribution may be explained by an angular variation of tensile load due to friction, which has been previously noted as a possible cause of strain variation within the gauge in the hemi arrangement [8].

When compared together, as shown on the left side of Figure 5, it is obvious that the YS and UTS have different values, with those of the dogbone method being lower than those for the hemi method. The resultant higher loads for the hemi method are likely due to friction counter acting the tensile load in the gauge region (described further in a following section), making the hemi test very sensitive to friction. The lower loads seen in the dogbone method are also likely caused by the stress concentrations and non-uniformity seen in the FE contours.

3.2 Parameter Variation Analysis

Building on these preliminary results of the base geometries, multiple parameters were varied according to the test matrix given in Table 2. The resulting normalized load-displacement plots are given below. For the dogbone method, parameters determined to have a significant effect on the load-displacement curves are shown in Figure 6 and those parameters with a minor effect are shown in Figure 7. For the hemi method, the plots for parameters with significant effects are given in Figure 8, and for parameters with minor effects in Figure 9. Again, these loads are normalized by the gauge cross-sectional area.[1]

For the dogbone, several parameters were classified as significant because they caused slope changes partway through the (otherwise) linear elastic region of the curves. Some of these effects are readily visible, like the difference in UTS for the eccentricity parameters in Figure 6. Others are less noticeable, like the ‘wobble’ and slope recovery for the -0.1mm dogbone diameter in Figure 6. While these differences are subtle and may not immediately stand out, they can nonetheless cause a significant

1 In the case of the eccentricity effect, the cross-sectional area is averaged across the length of the gauge.

uncertainty in measuring YS, which is determined by offsetting a line from this elastic region. Without a clear linear region (or with two distinct linear regions with separate slopes), reporting a 0.2% offset YS becomes subjective.

The resulting change in YS and UTS for each parameter variation was also measured. These changes, reported as a percentage of the original strength value, are given in a series of tables, from Table 4 to Table 15. Measurements are only given for parameters that were considered significant in one or both methods, i.e., where changing the parameter resulted in a change in YS or UTS of greater than 2%. These results confirmed the previous classification: ring inner diameter, gauge length, rotation, and eccentricity caused significant changes in the strength measurements of both the dogbone and hemi methods. Mandrel diameter, dogbone diameter, dogbone design angle, and ovality were also significant for the dogbone method only (hemi ovality is still included for comparison); and friction was found to be significant only for the hemi method (dogbone friction is still included for comparison). It is worth noting that an increase or decrease in measured strength compared to the original parameters is not inherently good or bad; it merely shows how sensitive the setup is to this parameter.

Several parameters in the dogbone method caused a change in YS of more than 5%, namely: a smaller gauge length (Table 5), smaller mandrel diameter (Table 6), larger dogbone diameter (Table 7), rotation of the ring relative to the dogbone (Table 9), and ovality with the minor axis located at the gauges (Table 13). Other dogbone method parameters resulted in a YS change of more than 10%: ring inner diameter variation (Table 4), and a smaller dogbone design angle (Table 8). Only the eccentricity, where the thin part of the ring was located at the top or bottom mandrel (90° from the midgauges), changed the UTS by more than 2% in the dogbone method. Conversely, in the hemi method only the coefficient of friction between the mandrel and the ring changed the YS by more than 5% or the UTS by more than 2% (Table 15).

Many of the parameters which had a noticeable effect on the dogbone YS related directly to the gaps between the ring and the fixturing grips. This aligns with the conclusions of Arsene and Bai's first introduction of the dogbone, that the gap plays a significant role [23]. The ring inner diameter, mandrel diameter, and dogbone diameter are the three parameters which directly define the gap between the fixtures and mandrels, and all three were found to be highly influential on the YS determination. These gaps in turn affect how much and what portion of the ring is supported by the dogbone insert. The rotation of the ring relative to the dogbone and the dogbone design angle (which also defines the arc length of the dogbone that contacts the ring) similarly affect how the insert supports the ring. As seen in Figure 5, the peak stress and strain tend to be located at the unsupported gap between fixturing, which suggests that these parameters are influential precisely because they directly impact how the ring is supported, and consequently where and to what degree a bending moment is experienced. The number of parameters that impact this gap, and the resulting YS measurement, makes the dogbone test particularly sensitive to small variations in test geometry, which are the hardest to control experimentally.

On the other hand, the hemi test method is comparatively robust to parameter variations. The primary exception is the significant impact of friction, which has a considerable influence on measured strengths (see Table 15). This parameter effect is unique in that it affected YS and UTS almost identically, and that varying the friction coefficient by the same increment causes roughly the same change in strength (roughly 6% strength change for ±0.05, 12% for ±0.10). This behavior is consistent with the expected behavior caused by friction lowering the tensile load in the gauge, which has been previously suggested [8]. If friction were to act opposite to the direction the gauge is pulled in, the resultant tensile load would decrease, and the tensile load would drop even further with increasing friction. That would mean that to experience the same true stress in the gauge, the mandrel load would have to be higher with higher coefficients of friction. In fact, this trend is clearly seen for the hemi in both Figure 8 and Table 15. The frictional effect is much less significant for the dogbone, as seen in Figure 7 and Table 15. This potential frictional behavior would also explain why the hemi normalized load was consistently higher than the dogbone normalized load in Figure 5: to achieve a similar true stress in the gauge (seen in the contours), the force of the mandrel would have to be much higher for the hemi method than for the dogbone method.

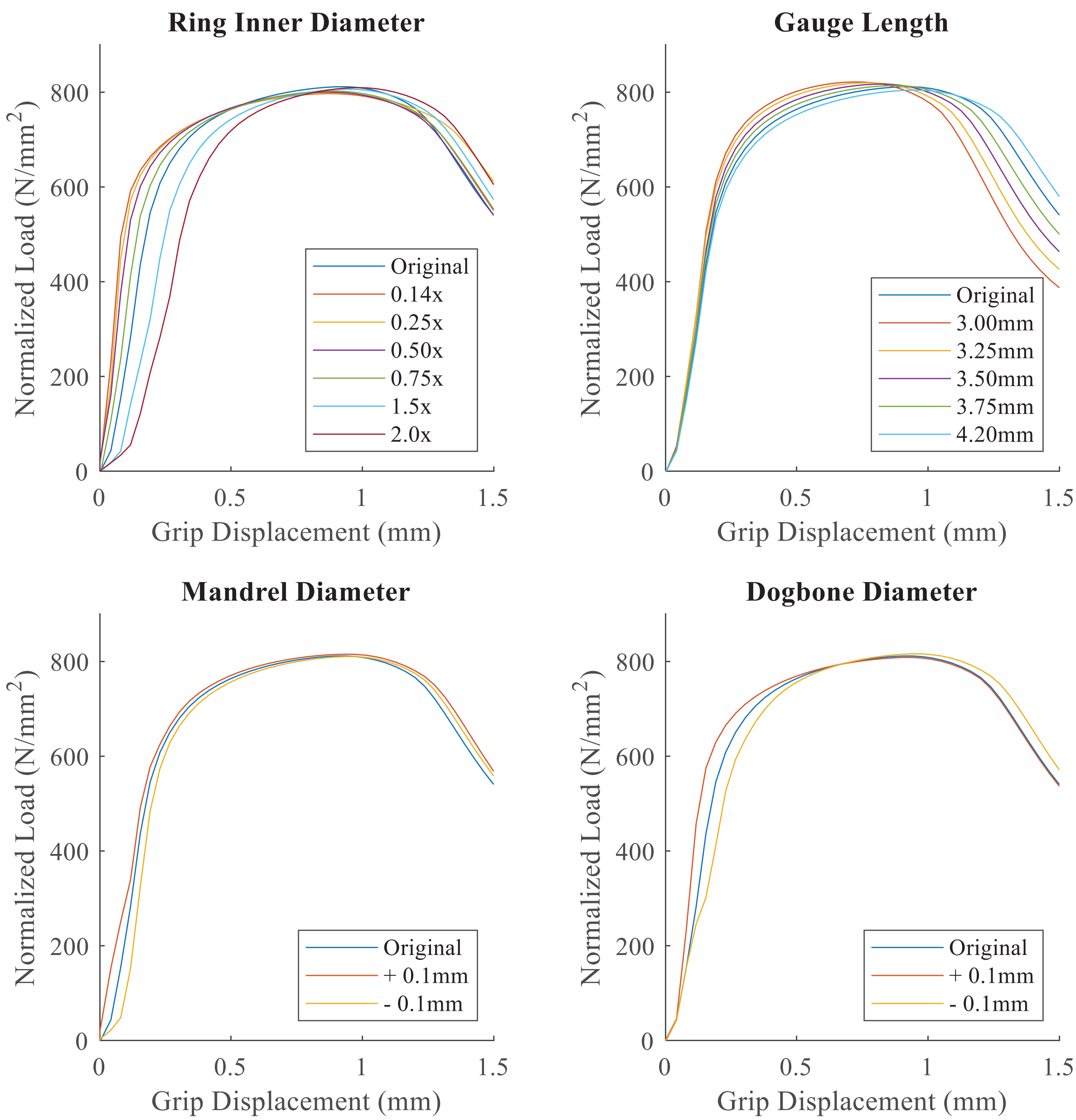

Ring Inner Diameter
Normalized Load (N/mm^2)
Grip Displacement (mm)
Original
0.14x
0.25x
0.50x
0.75x
1.5x
2.0x
Gauge Length
Normalized Load (N/mm^2)
Grip Displacement (mm)
Original
3.00mm
3.25mm
3.50mm
3.75mm
4.20mm
Mandrel Diameter
Normalized Load (N/mm^2)
Grip Displacement (mm)
Original
+ 0.1mm
- 0.1mm
Dogbone Diameter
Normalized Load (N/mm^2)
Grip Displacement (mm)
Original
+ 0.1mm
- 0.1mm

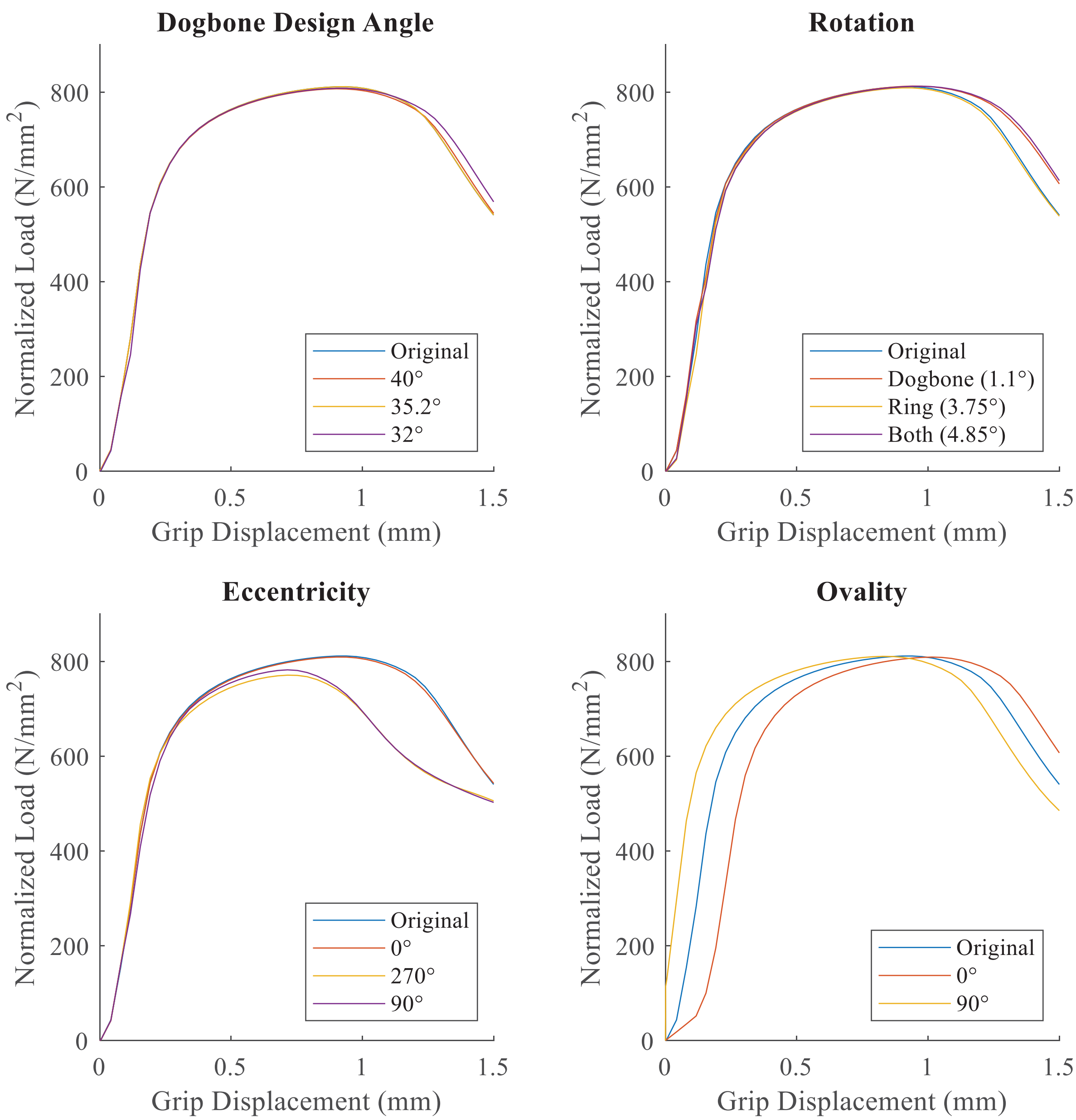

Figure 6. Dogbone method, significant parameter effects. Plots show normalized load vs displacement. Raw load is normalized by the cross-sectional area of the gauge region.

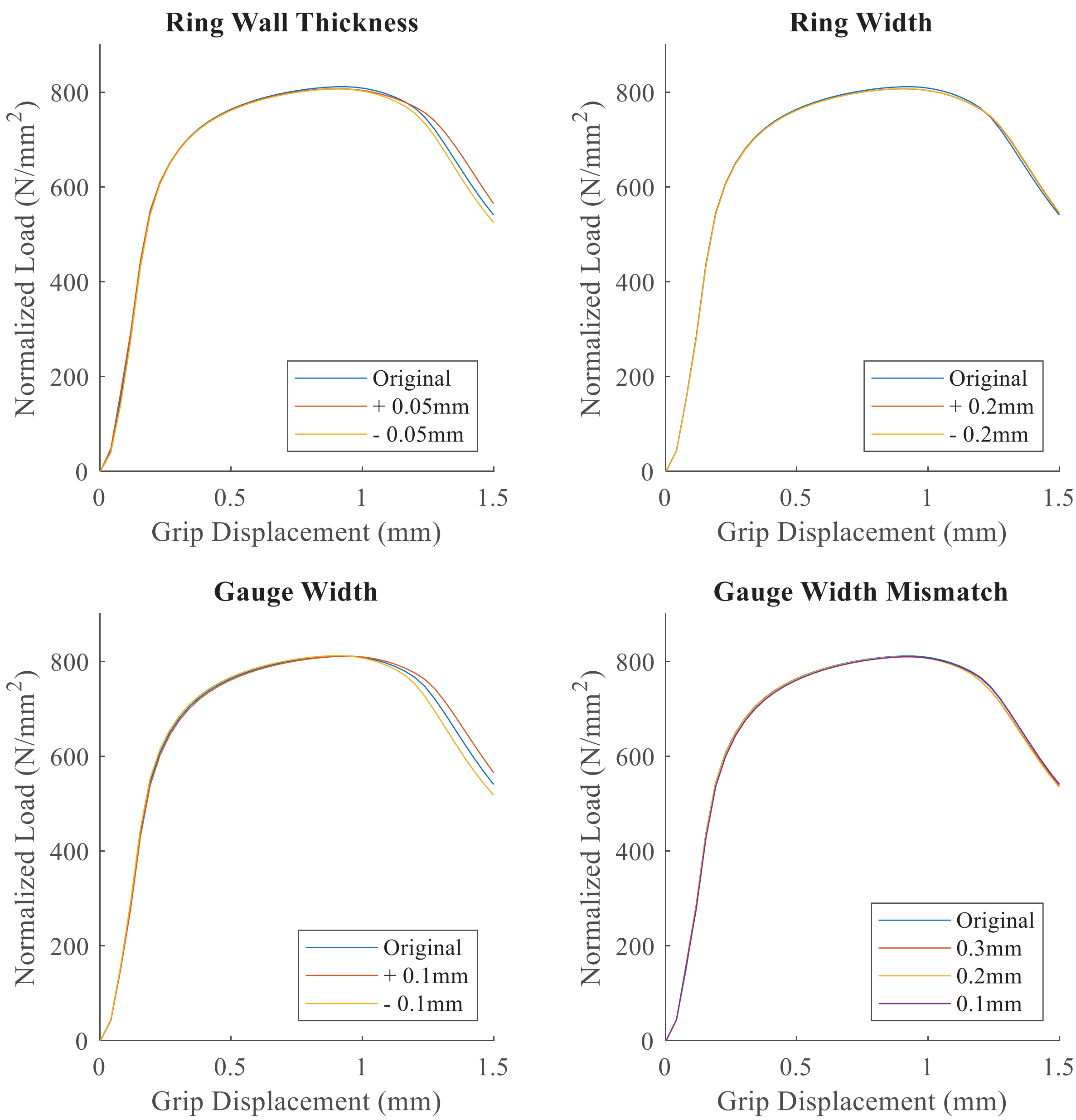
Ring Wall Thickness
Normalized Load (N/mm^2)
Grip Displacement (mm)
Original
+ 0.05mm
- 0.05mm
Ring Width
Normalized Load (N/mm^2)
Grip Displacement (mm)
Original
+ 0.2mm
- 0.2mm
Gauge Width
Normalized Load (N/mm^2)
Grip Displacement (mm)
Original
+ 0.1mm
- 0.1mm
Gauge Width Mismatch
Normalized Load (N/mm^2)
Grip Displacement (mm)
Original
0.3mm
0.2mm
0.1mm

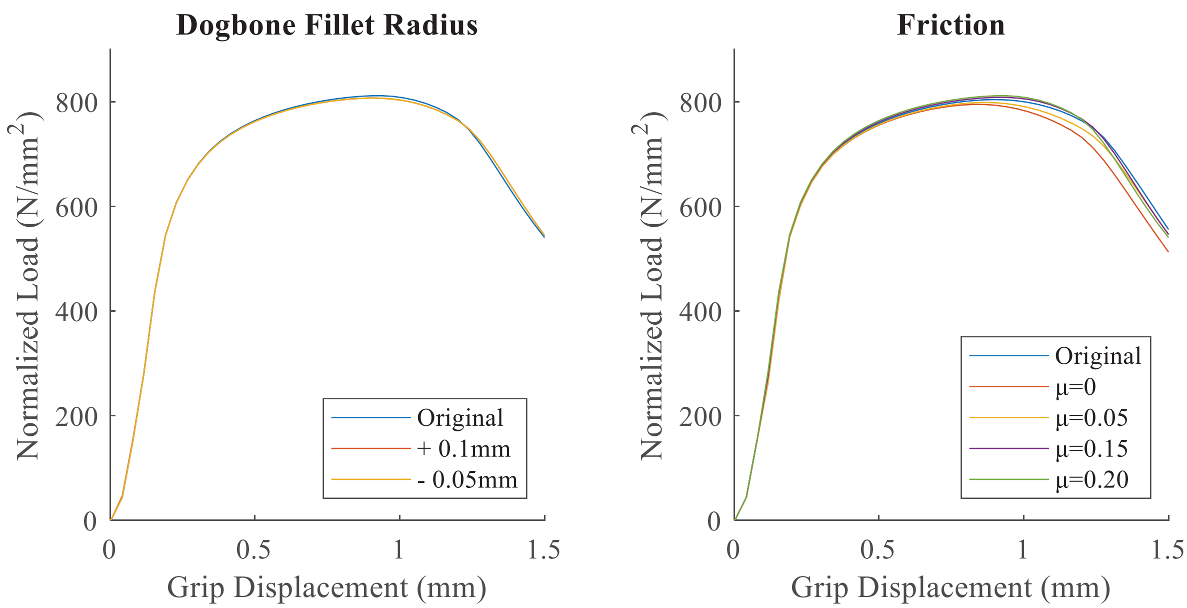

Figure 7. Dogbone method, minor parameter effects. Plots show normalized load vs displacement. Raw load is normalized by the cross-sectional area of the gauge region.

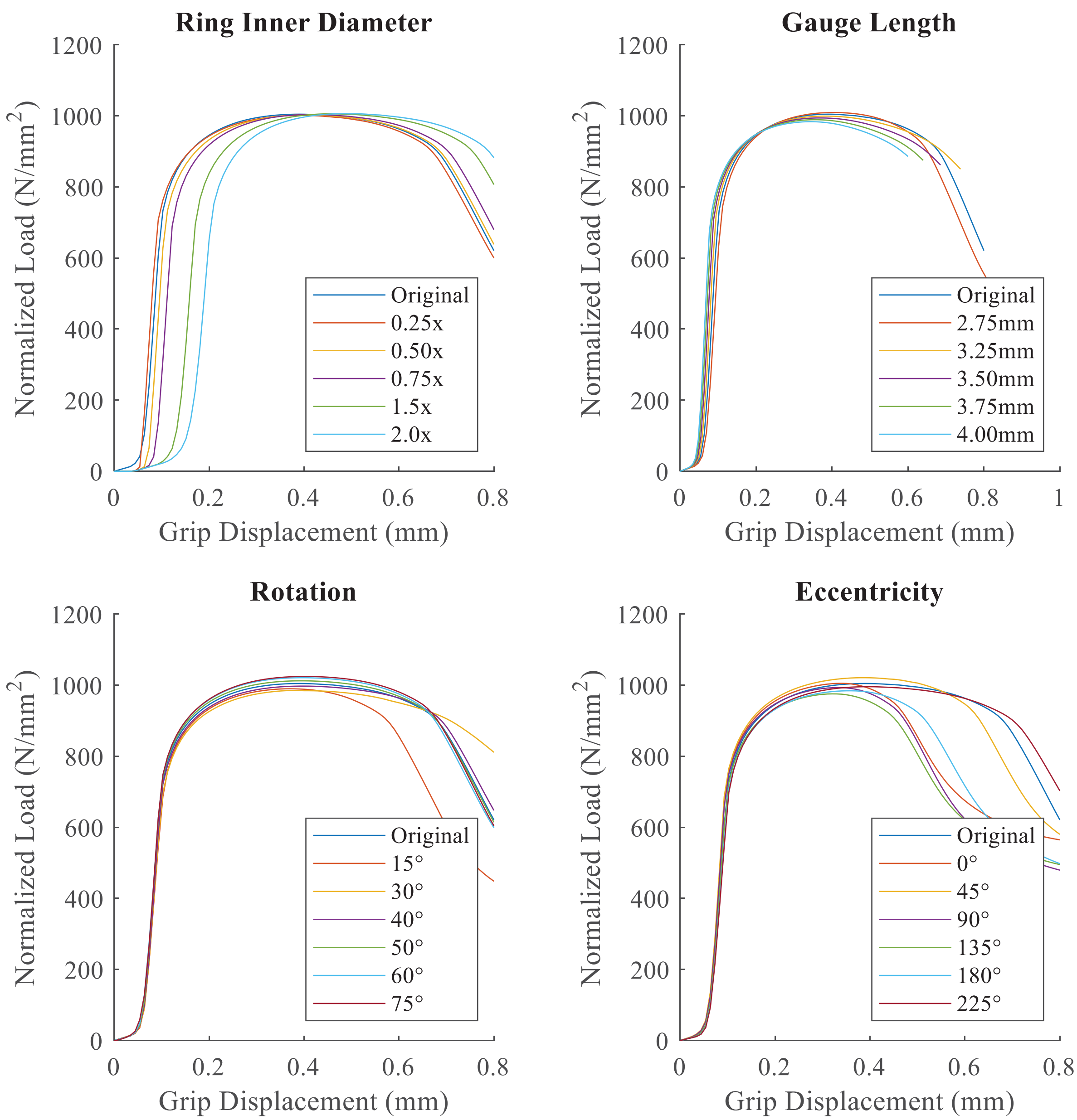

Ring Inner Diameter
Normalized Load (N/mm^2)
Grip Displacement (mm)
Original
0.25x
0.50x
0.75x
1.5x
2.0x
Gauge Length
Normalized Load (N/mm^2)
Grip Displacement (mm)
Original
2.75mm
3.25mm
3.50mm
3.75mm
4.00mm
Rotation
Normalized Load (N/mm^2)
Grip Displacement (mm)
Original
15°
30°
40°
50°
60°
75°
Eccentricity
Normalized Load (N/mm^2)
Grip Displacement (mm)
Original
0°
45°
90°
135°
180°
225°

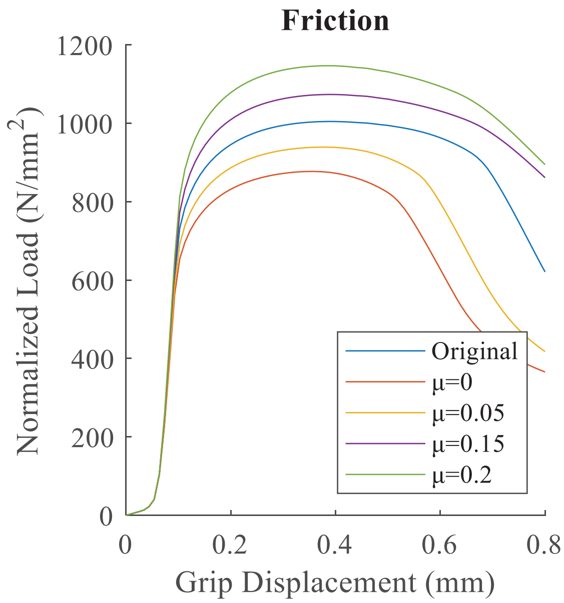

Figure 8. Hemi method, significant parameter effects. Plots show normalized load vs displacement. Raw load is normalized by the cross-sectional area of the gauge region.

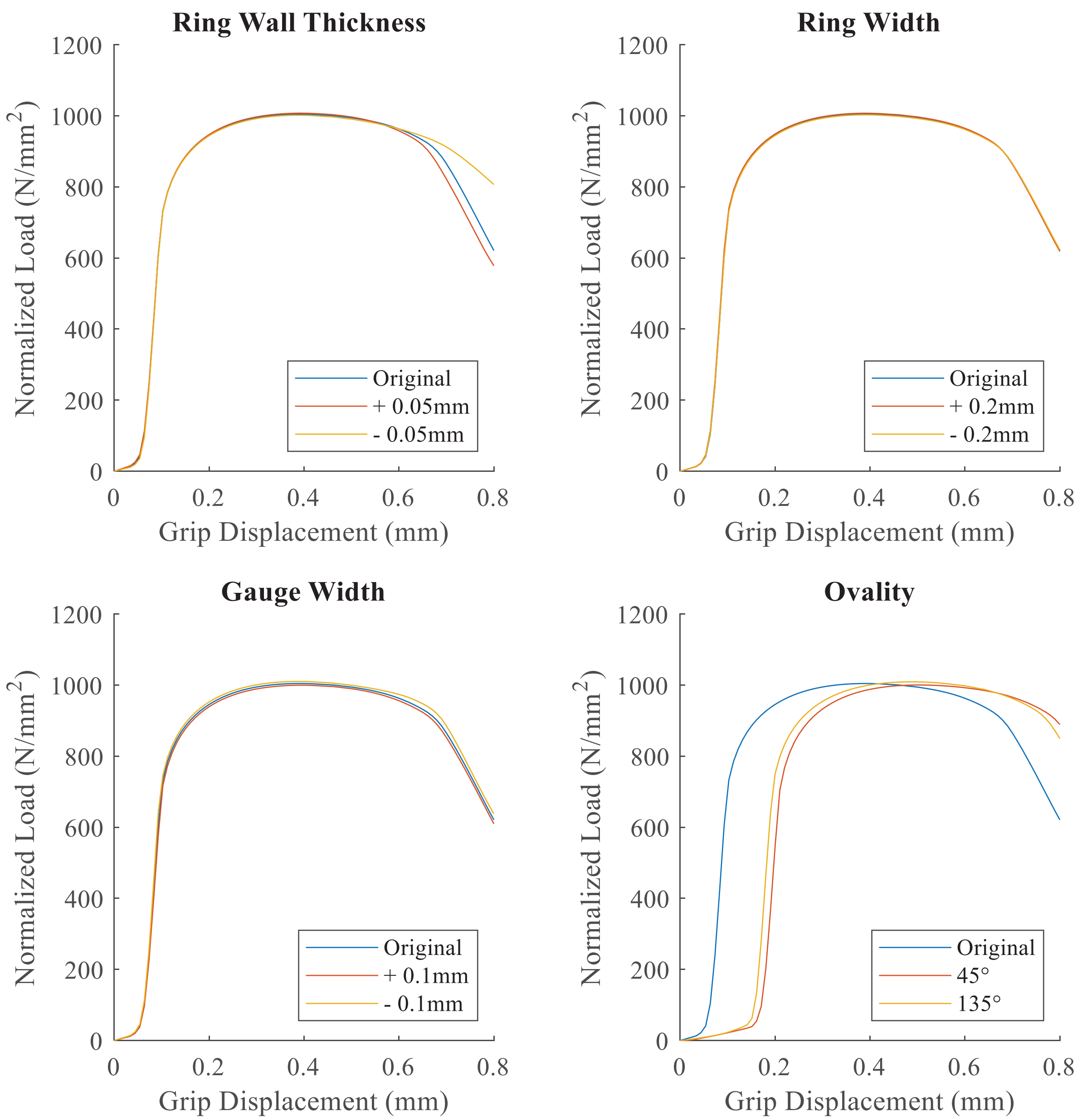

Figure 9. Hemi method, minor parameter effects. Plots show normalized load vs displacement. Raw load is normalized by the cross-sectional area of the gauge region.

Table 4. Dogbone and Hemi comparison of measured strengths for various ring inner diameters, reported by the change in the size of gap between the ring and fixturing relative to the original. Strengths are from

load-displacement curves normalized by gauge cross-sectional area and length but are otherwise uncorrected.

Ring ID, size of gap		0.14x	0.25x	0.50x	0.75x	Original	1.5x	2.0x
Dogbone	YS change	-4.1%	-11.1%	-12.0%	-8.6%	N/A	+6.3%	+10.8%
	UTS change	-0.9%	-0.7%	-0.5%	-0.2%	N/A	+0.3%	+0.7%
Hemi	YS change		-2.5%	-2.3%	-1.1%	N/A	+0.6%	+1.2%
	UTS change		-0.3%	-0.2%	-0.1%	N/A	+0.1%	+0.1%

Table 5. Dogbone and Hemi comparison of measured strengths for various gauge lengths. Strengths are from load-displacement curves normalized by gauge cross-sectional area and length but are otherwise uncorrected.

Gauge Length		2.75mm	3.00mm	3.25mm	3.50mm	3.75mm	4.00mm	4.20mm
Dogbone	YS change		+5.8%	+3.4%	+4.4%	+1.5%	N/A	-1.5%
	UTS change		+1.3%	+1.1%	+0.7%	+0.4%	N/A	-0.8%
Hemi	YS change	0%	N/A	+0.1%	-0.4%	-1.1%	-1.7%	
	UTS change	+0.5%	N/A	-0.5%	-1.0%	-1.5%	-2.1%	

Table 6. Comparison of measured strengths for changes in mandrel diameter with the dogbone method. Strengths are from load-displacement curves normalized by gauge cross-sectional area and length but are otherwise uncorrected.

Mandrel Diameter		+0.1mm	Original	-0.1mm
Dogbone	YS change	-3.8%	N/A	-6.6%
	UTS change	+0.5%	N/A	-0.1%

Table 7. Comparison of measured strengths for changes in dogbone insert diameter with the dogbone method. Strengths are from load-displacement curves normalized by gauge cross-sectional area and length but are otherwise uncorrected.

Dogbone Diameter		+0.1mm	Original	-0.1mm
Dogbone	YS change	-6.4%	N/A	+0.4%
	UTS change	-0.3%	N/A	+0.6%

Table 8. Comparison of measured strengths for changes in dogbone design angle with the dogbone method. Strengths are from load-displacement curves normalized by gauge cross-sectional area and length but are otherwise uncorrected.

Dogbone Design Angle		+6.4°	+1.6°	Original	-1.6°
Dogbone	YS change	+0.3%	+0.2%	N/A	-10.4%
	UTS change	-0.5%	+0.1%	N/A	-0.3%

Table 9. Comparison of measured strengths for rotations of the dogbone method setup, including the dogbone only, the ring only, and the dogbone and ring combined rotation. Strengths are from load-displacement curves normalized by gauge cross-sectional area and length but are otherwise uncorrected.

Rotation		Original	Dogbone, 1.1°	Ring, 3.75°	Both, 4.85°
Dogbone	YS change	N/A	+2.1%	-6.4%	+0.6%
	UTS change	N/A	+0.2%	-0.3%	+0.2%

Table 10. Comparison of measured strengths for rotation of the ring in the hemi method. Strengths are from load-displacement curves normalized by gauge cross-sectional area and length but are otherwise uncorrected.

Rotation		15°	30°	40°	Original	50°	60°	75°
Hemi	YS change	-0.3%	-2.3%	+0.2%	N/A	+0.5%	+1.5%	+1.6%
	UTS change	-1.5%	-1.9%	-0.7%	N/A	+0.8%	+1.6%	+2.0%

Table 11. Comparison of measured strengths for various orientations of an eccentric ring with the dogbone method. Strengths are from load-displacement curves normalized by gauge cross-sectional area and length but are otherwise uncorrected.

Eccentricity, Location of thinnest part		Original	0°	90°	270°
Dogbone	YS change	N/A	-1.0%	-1.1%	-1.3%
	UTS change	N/A	-0.2%	-3.5%	-4.9%

Table 12. Comparison of measured strengths for various orientations of an eccentric ring with the hemi method. Strengths are from load-displacement curves normalized by gauge cross-sectional area and length but are otherwise uncorrected.

Eccentricity, Location of thinnest part (relative to gauge)		Original (N/A)	0° (-45°)	45° (0°)	90° (45°)	135° (90°)	180° (135°)	225° (180°)
Hemi	YS change	N/A	+0.4%	+0.8%	-0.3%	-0.9%	-0.4%	-0.4%
	UTS change	N/A	+0.1%	+1.6%	-1.1%	-2.9%	-2.0%	-0.9%

Table 13. Comparison of measured strengths for orientations of a slightly oval ring with the dogbone method. Strengths are from load-displacement curves normalized by gauge cross-sectional area and length but are otherwise uncorrected.

Ovality, Location of major axis		Original	0°	90°
Dogbone	YS change	N/A	+0.5%	-7.5%
	UTS change	N/A	-0.2%	0%

Table 14. Comparison of measured strengths for orientations of a slightly oval ring with the hemi method. Strengths are from load-displacement curves normalized by gauge cross-sectional area and length but are otherwise uncorrected.

Ovality, Location of major axis (relative to gauge)		Original (N/A)	45° (0°)	135° (90°)
Hemi	YS change	N/A	+0.6%	+0.6%
	UTS change	N/A	-0.4%	+0.5%

Table 15. Comparison of measured strengths for a variety of friction coefficients between the fixturing and ring with both the dogbone and hemi methods. Strengths are from load-displacement curves normalized by gauge cross-sectional area and length but are otherwise uncorrected.

Friction		μ=0	μ=0.05	Original	μ=0.15	μ=0.20
Dogbone	YS change	+1.2%	-1.1%	N/A	-0.4%	-1.7%
	UTS change	-1.2%	-0.7%	N/A	+0.5%	+0.9%
Hemi	YS change	-12.4%	-6.5%	N/A	+6.8%	+14.2%
	UTS change	-12.7%	-6.5%	N/A	+6.9%	+14.2%

3.3 Correction Factors

Ultimately, the key criterion in selecting a RTT method is the ability to extract accurate material properties from the tests. From Figure 5, a significant discrepancy between the two test methods is apparent: when using only raw normalized load-apparent strain data, the hemi method predicts much higher strengths than the dogbone method. Table 16 shows the calculated strengths from the raw dogbone and hemi data, compared to the known values of the finite element model material input. The table also shows strength values calculated from the raw hemi data using three additional correction methods, which will be discussed later in this section. This shows that the dogbone underpredicts both strengths and the hemi overpredicts both strengths. While the raw dogbone method results are closer to the correct values and more conservative than the raw hemi method results, both methods lead to significant strength measurement errors when using the raw, uncorrected data. Thus, the ability to pair the test with predictable, reliable correction factors that can be applied to a variety of testing conditions is critical in determining highly accurate material strength properties.

In this regard, the stress states shown in Figure 5 suggest that the hemi method is better suited to a correction factor than the dogbone method. As previously noted, the hemi method contour closely mimics the uniform, uniaxial stress state that would be exhibited in a traditional tensile test. When the Figure 5 contours and the parameter variation results are considered together, it is apparent that mandrel-ring friction likely explains the hemi method's overprediction, while premature yielding and non-uniform stresses in the gauge likely explain the dogbone method's underprediction. Correction schemes have been developed for measuring strengths in the dogbone method [10], [12] and for the smaller mandrel method, which also exhibits a more complicated non-uniaxial stress state [21], [22]. However, these schemes are empirically derived from finite element modeling, either from a single setup or from several setups spanning a select range of geometries and materials. While these corrections have shown improvement in the ability to determine some strength properties, the empirical approach necessarily limits their broader applicability to the selected range of parameters used to develop the empirical model, limiting the potential for accurate strength measurements. On the other hand, the uniform uniaxial stress state of the hemi method shows great promise for accurate corrections. Developing a mechanistic explanation for hemi method strength overprediction that remains unchanged for a variety of test geometries and materials would lead to a broadly applicable correction scheme, resulting in unbiased strength measurements.

Table 16. Comparison of strengths from the FE model material input, measurements of the raw dogbone and hemi data, and measurements with various correction methods.

	YS (MPa)	UTS (MPa)
Material Model (Correct)	626	846
Raw Dogbone (% error)	562 (-10.1%)	811 (-4.1%)
Raw Hemi (% error)	751 (+22.4%)	1005 (+18.8%)
Symmetric Correction Hemi, using Equation 3 (% error)	708 (+13.1%)	929 (+9.8%)
Asymmetric Correction Hemi, using Equation 9 (% error)	667 (+6.5%)	873 (+3.1%)
Contact Correction Hemi, using Equation 15 (% error)	630 (+0.7%)	843 (-0.4%)

In developing this mechanics-based correction factor for the hemi method, the logical first step is an investigation of the most sensitive parameter: friction. From Table 15, the effect of changing friction coefficients on strength values in the hemi method follows a predictable pattern. The inherent uniformity of the stress and strain in the hemi test also makes it an ideal candidate for such a correction factor; while the dogbone underpredicts strength because of non-uniformity, the hemi test stress distribution is close to a traditional uniaxial tension test. Thus, a correction factor applied to the measured mandrel load in a hemi test would result in a corrected force that closely represents the entire gauge. This assumption does not hold for the dogbone test, where the combined tension and bending moment loading result in a more complex, less uniform stress state. To formulate such a friction correction factor for the hemi method, a thorough understanding of how the load varies in the ring is essential.

Previous efforts have been made to account for the effect of friction on the load in the hemi RTT. Dick and Korkolis used the capstan equation, or Eytelwien's formula, to describe the variation of the ring's internal tensile load as a function of the angle from the mandrel edge (the gap between the two mandrels, see Figure 4). This relationship is given in Equation 1, where N_g is the tensile load at the gauge-side gap ($\theta = 0$), μ is the coefficient of friction, and θ is the angle in radians[2]. They concluded that for the case where $\mu = 0.1$, which is the modeled value of friction, the drop in force at 90° would be 15%, and the variation across the 30° span of their designed gauge would be less than 5% [8]. This assumes that the relationship holds for the entirety the quarter circle, to 90°. The average load carried by the gauge can be calculated using the angle-dependent load, as in Equation 2a. If the load is also assumed to be evenly distributed to both sides of the ring and in turn the tensile load at both sides of the gap are equal ($N_g = N_r = 0.5\ N_{grip}$, where N_r is the tensile force at the ring-side gap at θ =180°), then the average load for the gauge could be determined using Equation 2b, where θ_1 and θ_2 are the respective ends of the gauge region. Implementing this equation results in a symmetric force correction factor (Equation 3), which can be multiplied by twice the raw strength to generate the symmetric correction hemi strengths reported in Table 16 (see Equation 4a and b). While these strength values are closer to the correct material values, this treatment of friction doesn't perfectly describe the behavior of the ring.

$$N(\theta) = N_g e^{-\mu\theta} \quad \text{(Eq. 1)}$$

[2] For use in this and subsequent equations, angles should be in radians. However, for ease-of-use angles in the text have been reported in degrees.

$$N_{gauge,avg} = \frac{\int_{\theta_1}^{\theta_2} N(\theta) d\theta}{(\theta_2 - \theta_1)} \quad \text{(Eq. 2a)}$$

$$N_{gauge,avg} = \int_{\theta_1}^{\theta_2} 0.5\ N_{grip}\ e^{-\mu\theta} d\theta / (\theta_2 - \theta_1), \quad where\ 0 < \theta < \pi \quad \text{(Eq. 2b)}$$

$$C_{symm} = \frac{N_{gauge,avg}}{N_{grip}} = \frac{e^{-\mu\theta_1} - e^{-\mu\theta_2}}{2\ \mu\ (\theta_2 - \theta_1)} \quad \text{(Eq. 3)}$$

$$YS_{symm} = 2\ YS_{raw}\ C_{symm} \quad \text{(Eq. 4a)}$$

$$UTS_{symm} = 2\ UTS_{raw}\ C_{symm} \quad \text{(Eq. 4b)}$$

An investigation of the frictional forces at the ring-surface interface in the gauge helps to explain why the symmetric friction correction factor fails to adequately correct for the material values. Figure 10 shows a vector plot of the resultant frictional shear forces in the gauge region, at the finite element analysis steps corresponding to yield stress and ultimate tensile stress identified from the stress-strain curve. This plot confirms that friction is acting primarily in the hoop direction, opposite to the direction of motion, which would cause the reduction of tensile load described by Equation 1. However, it also demonstrates that the assumption of symmetry about the y-z plane does not hold. In previous work on the hemicylindrical test method, friction was assumed to cause the tensile load to decrease from $\theta = 0$ to $\theta = 90°$, i.e., Equation 1 holds, and $N_g = N_r$. By extension, this assumes that moving from $\theta = 90°$ to $\theta = 180°$, the tensile force would stop decreasing and begin increasing again. It follows that the point where the direction of the frictional force resisting deformation inflects (previously assumed to be $\theta = 90°$), would also be the location that stays stationary on the ring (the point is essentially fixed, relative to the mandrel). However, Figure 10 shows that this friction inflection point doesn't occur at 90°; when yielding begins, this fixed point is roughly 51°, and at the advanced deformation stage of UTS it is at 45°, or the midgauge position.

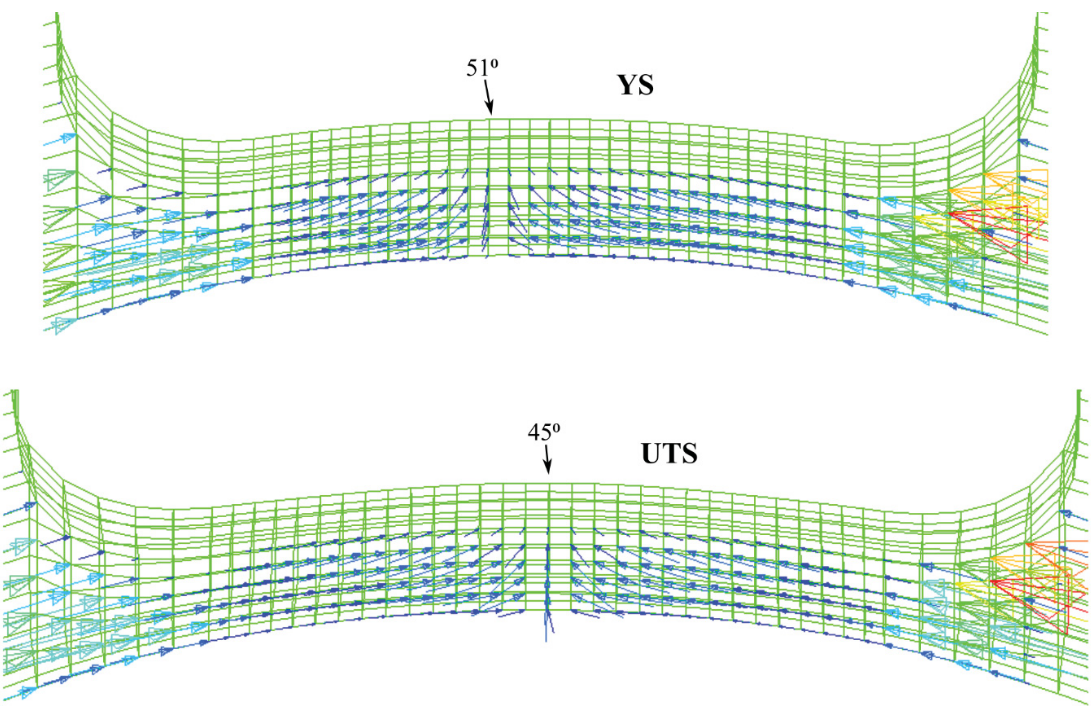

Figure 10. Diagram showing resultant vectors of frictional shear force plotted on the hemi gauge region, at model increment corresponding to YS and UTS. The angle location where vectors converge is noted.

To better understand the variation of tensile force in the ring, free body cuts of the finite element model were used to determine the tensile load at a range of angles from 0 to 180°, where the center of the gauge is located at 45°. A cylindrical material coordinate system was used in the model so that the free body cuts would report forces in the hoop direction, regardless of angle. The free body cut data (solid blue line) in Figure 11 show the hoop tensile force as function of the angular location in the ring; the location of the ends of the gauge are shown (vertical dotted gray lines). This plot of the actual tensile force carried by the ring, can be compared to the tensile load predicted by a variety of correction methods, also shown in Figure 11. The horizontal line (solid red line) shows the uncorrected force profile from the raw load-displacement curve corresponding to the raw hemi results in Table 16 and the previous plots in this paper. The symmetric correction, which uses Equation 2 and assumes symmetry about 90°, is also shown with its V-shaped force profile (yellow dashed line). It is readily apparent that the free body cut forces at $\theta = 0$ and $\theta = 180°$ are not the same, i.e., $N_g \neq N_r$, and that the tensile force in the ring is not symmetric at 90°. Rather, the force at the gauge-side gap, N_g, is lower than the ring-side gap, N_r. An inflection point in the free body cut force profile is also visible, at roughly 51° for the YS step and at roughly 45° for the UTS step. These inflection points match closely with the fixed points seen in Figure 10, giving additional confirmation that the variation of the force profile shown in the free body cuts is related to the frictional forces between the mandrel and ring. It is also notable that the slope of the symmetric correction force profile matches the free body cut force profile very well. Although the inflection point is different for the two, both left sides are parallel with each other, as are the right sides. This also gives confidence that the relationship described in Equation 1 holds, but the assumptions about symmetry do not.

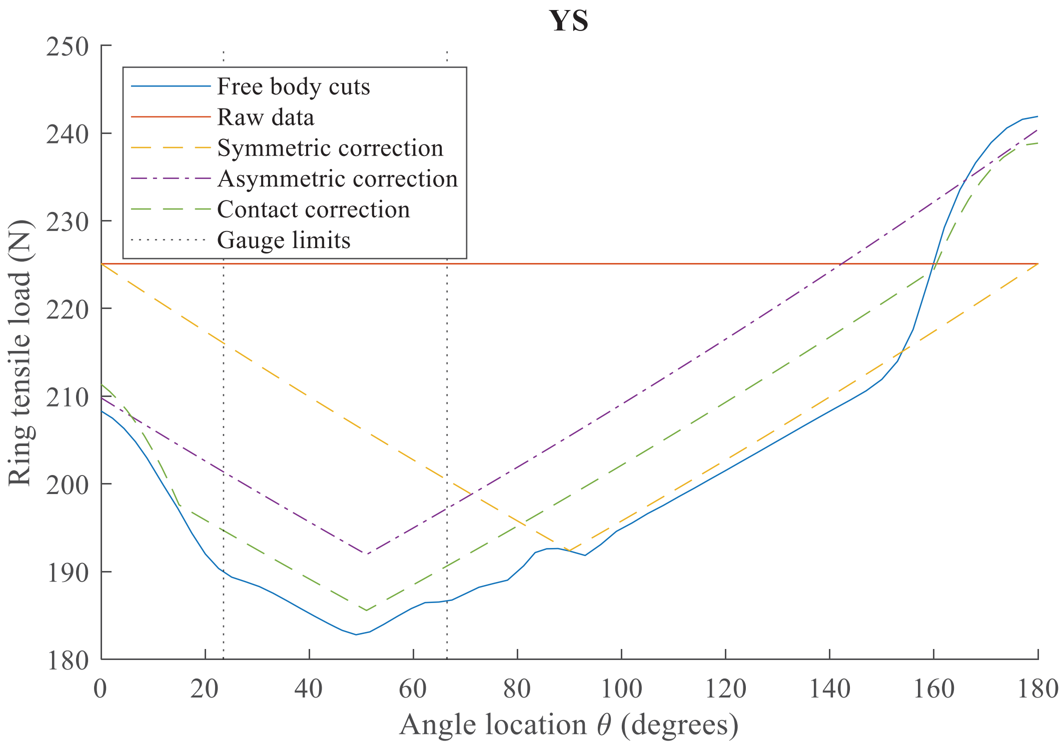

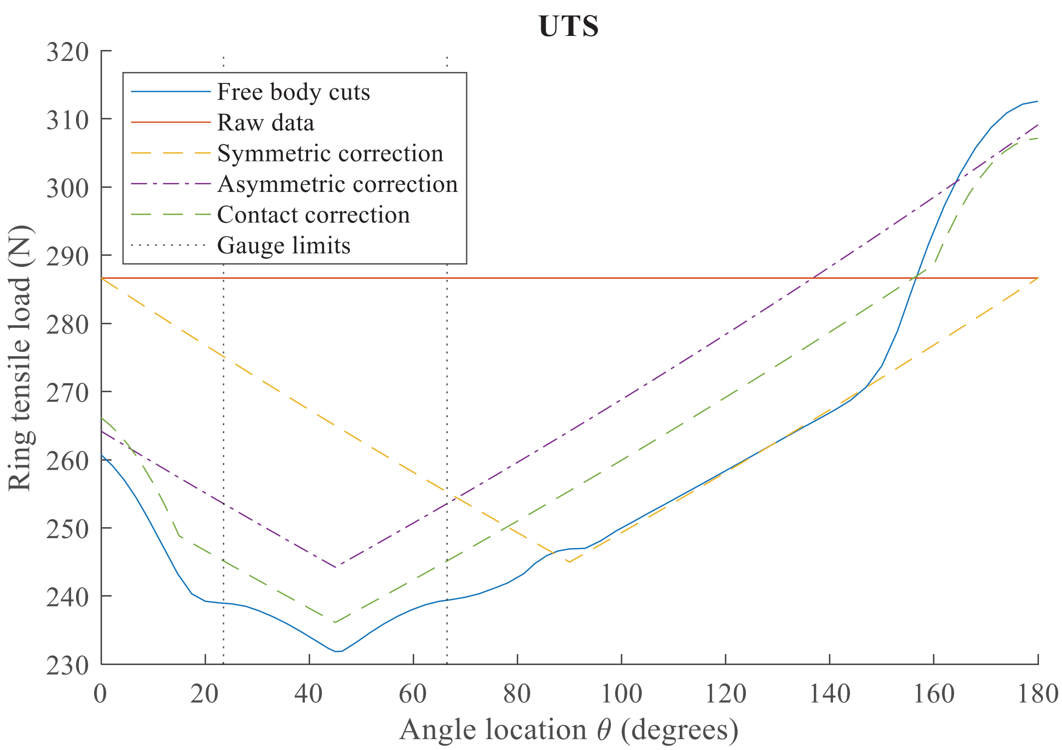

Figure 11. Plot of ring tensile load as a function of angle at YS and UTS determined with free body cuts, compared to a variety of load correction schemes: raw data (half of mandrel force), friction correction assuming symmetry, friction correction assuming asymmetry, and friction correction assuming asymmetry and accounting for contact.

Based on this understanding, a more precise asymmetric model to describe the distribution of the force can be formulated. Assuming the relationship between friction and tensile force of Equation 1 still holds, the force profile can be described by the piecewise function of Equation 5, where θ_f is the fixed location relative to the mandrel (where the frictional force changes direction).

$$N(\theta) = N_g\, e^{-\mu\theta} \qquad for\ 0 < \theta \leq \theta_f$$

$$N(\theta) = N_r\, e^{-\mu(\pi-\theta)} \qquad for\ \theta_f < \theta < \pi \tag{Eq. 5}$$

To ensure the tensile force profile is continuous at the fixed location inflection point, Equation 6a is imposed, leading to the relationship between the forces at the two sides in Equation 6b. Then, because the forces in the ring must sum to the mandrel force (Equation 7a-7c), the forces at both gaps are given by Equation 8a and 8b, which define the force distribution of Equation 5.

$$N_g\, e^{-\mu\theta_f} = N_r\, e^{-\mu(\pi-\theta_f)} \tag{Eq. 6a}$$

$$\frac{N_g}{N_r} = e^{-\mu(\pi-2\theta_f)} \tag{Eq. 6b}$$

$$N_{mandrel} = N_g + N_r \tag{Eq. 7a}$$

$$N_g N_{mandrel} = N_g N_g + N_g N_r \tag{Eq. 7b}$$

$$\frac{N_g}{N_r} N_{mandrel} = N_g\left(1 + \frac{N_g}{N_r}\right) \tag{Eq. 7c}$$

$$N_g = N_{mandrel}\ \frac{1}{1+e^{\mu\left(\pi-2\theta_f\right)}} \tag{Eq. 8a}$$

$$N_r = N_{mandrel}\left(\frac{1}{1+e^{-\mu\left(\pi-2\theta_f\right)}}\right) \tag{Eq. 8b}$$

To find the average force in the gauge, the piecewise function is integrated across the range of gauge angles, and then is divided by the angle span, as in Equation 2a. This piecewise function is found by inserting Equations 8a and 8b into Equation 5. This yields the asymmetric force correction factor in Equation 9.

$$C_{asymm} = \frac{e^{\mu(\theta_2-2\theta_f)}+e^{-\mu\theta_1}-2e^{-\mu\theta_f}}{\mu(\theta_2-\theta_1)\left(1+e^{\mu\left(\pi-2\theta_f\right)}\right)} \tag{Eq. 9}$$

This asymmetric force correction factor relies on the friction coefficient μ, the angle locations at either end of the gauge θ_1 and θ_2, and the fixed location point θ_f. This fixed location point depends on both the ring geometry and on the stage of deformation. At any mandrel displacement, this fixed point will be located at the point on the ring where the elongation to either side is equal. This is shown in Figure 12; for the fixed point, Equation 10 is true, assuming the displacement of the mandrel $\delta_{mandrel}$ is completely vertical and that the mandrel is constrained from rotation or side-to-side motion. If this is the case, then at UTS where elongation of the ring is dominated by the gauge, it follows that the point θ_f will be located at the midgauge, or 45° (π/4 radians). This is confirmed by both Figure 10 and Figure 11.

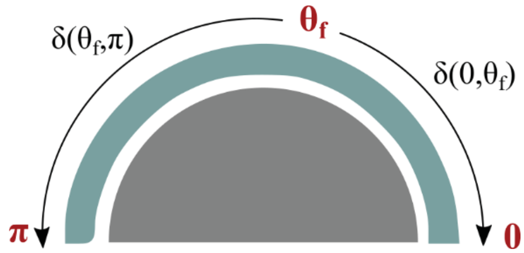

Figure 12. Schematic showing location of fixed point, θ_f, with equal elongation on either side.

$$\delta(0, \theta_f) = \delta(\theta_f, \pi) = \frac{1}{2}\delta_{mandrel} \qquad \text{(Eq. 10)}$$

However, as seen by Figure 10, the fixed location is not at the final location during the range of ring deformations. Prior to yielding, there is a greater contribution of the non-gauge part of the ring to the deformation. In this case, the angle location of the fixed point is in between the midgauge and the end of the gauge region. The exact location is determined by the geometry of the gauge and ring. In this case, we can use the midgauge angle at YS and the 51° from Figure 10 at UTS to fully define the force profile. This is plotted as the asymmetric correction in Figure 11 (purple dash-dotted line) and is used along with Equation 9 to calculate the asymmetric corrected strengths in Table 16. It is worth noting that, although less accurate, assuming the fixed point is the midgauge at 45° rather than 51° changes the strength results by roughly 0.2%. When compared to other sources of uncertainty, the error introduced by this assumption is essentially negligible. Overall, the corrected strengths are closer to the true values than the dogbone test strengths, although they are still an overestimate, while the dogbone is conservative.

The force profile of Figure 11 and the results of Table 16 demonstrate the significant improvement of the asymmetric correction in both modeling the tensile load and measuring strength values. However, it also shows that this correction doesn't fully describe the behavior of the tensile load as measured by the free body cuts. Near θ = 0 and θ = 180°, the free body cuts (solid blue lines) show a curved sinusoidal-type profile, distinct from the friction-dominated profile. At these extreme angles, the ring does not contact the entire surface of the mandrel. Rather, as seen in Figure 13, the locations θ_{rc} and θ_{gc} where full contact has been developed (meaning the line of nodes where all surrounding elements have some contact) are offset from θ = 0 and θ = 180°. These locations of full contact correspond closely to the angles at which the free body cut plot in Figure 11 transitions from the sinusoidal-type profile (concave down curve) to the friction-defined profile (the V-shape). This apparent switch in behavior is not unexpected; from θ = 0 to θ_{gc} and again from θ_{rc} to θ = 180°, the ring is unsupported by the mandrel, therefore the tensile load profile is not dominated by friction over these spans.

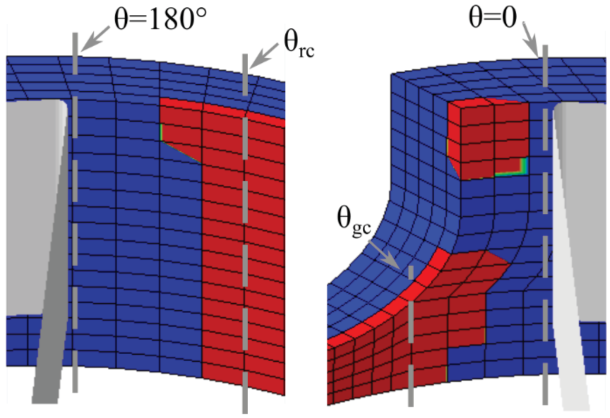

Figure 13. Regions of contact in finite element model at yield point. Elements in contact with the mandrel are shown in red, elements not in contact are shown in blue. Dashed lines show θ = 0 and θ = 180°, as well as the locations where full contact has been developed, θ_{rc} and θ_{gc}. The upper mandrel has been removed for visibility, but the lower mandrel has been included for reference.

This can easily be understood by the force balance diagram in Figure 14. As the angle varies, the tensile force is simply the hoop component of the resultant force at the gap. It is important to note that based on the free body cuts performed previously, a radial component $N_{g,radial}$ was found at the gauge-side gap where θ = 0, which is nearly the same as the horizontal component of the mandrel reaction force. However, little to no radial component was found at the ring-side gap where θ = 180°, so $N_{r,radial} \approx 0$. It follows that the tensile load over this unsupported region is dictated by the orientation of the component vectors. The locations of contact at the gauge-side (θ_{gc}) and at the ring-side (θ_{rc}) become the points where the tensile load behavior transitions from following a component-defined to a friction-defined behavior. The full contact corrected behavior of tensile forces in the ring are described by the piecewise function given in Equation 11, which is an expanded version of Equation 5. Note that the forces over the friction-dominant range are defined by the hoop force components at the locations of contact, N_{gc} and N_{rc}, and α is the ratio of the radial to hoop force component at the gauge-side gap ($N_{g,radial}/N_{g,hoop}$ as seen in Figure 14).

$$N(\theta) = N_g(\cos(\theta) - \alpha\sin(\theta)) \qquad for\ 0 < \theta \le \theta_{gc}$$

$$N(\theta) = N_{gc}\, e^{-\mu(\theta-\theta_{gc})} \qquad for\ \theta_{gc} < \theta \le \theta_f$$

$$N(\theta) = N_{rc}\, e^{-\mu(\theta_{rc}-\theta)} \qquad for\ \theta_f < \theta \le \theta_{rc}$$

$$N(\theta) = N_r\cos(\pi - \theta) \qquad for\ \theta_{rc} < \theta \le \pi \qquad \text{(Eq. 11)}$$

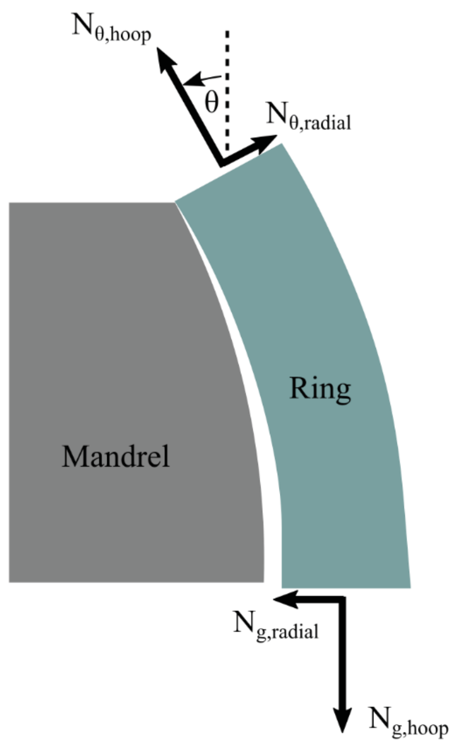

Figure 14. Force diagram of the unsupported portion of the ring near the gauge-side of the ring. The forces of a section cut located at angle $0 < \theta < \theta_{gc}$ are shown in their radial and hoop components at the top of the figure, and the components at the gauge-side gap are shown at the bottom.

As with the derivation of the asymmetric correction method, the continuity condition at the fixed point can be used to define a relationship for N_{gc} and N_{rc} shown in Equation 12. Then using the first and last piece of Equation 11, one can relate N_g and N_r as shown in Equation 13. Then because the forces must balance with the mandrel force (see Equation 7a through 7c), this leads to the gap forces as a function of the mandrel force shown in Equation 14a and 14b.

$$N_{gc}\, e^{-\mu(\theta_f-\theta_{gc})} = N_{rc}\, e^{-\mu(\theta_{rc}-\theta_f)} \quad \text{(Eq. 12a)}$$

$$\frac{N_{gc}}{N_{rc}} = e^{\mu(2\theta_f-\theta_{gc}-\theta_{rc})} \quad \text{(Eq. 12b)}$$

$$\frac{N_g}{N_r} = e^{\mu(2\theta_f-\theta_{gc}-\theta_{rc})}\frac{\cos(\pi-\theta_{rc})}{\cos(\theta_{gc})-\alpha\sin(\theta_{gc})} \quad \text{(Eq. 13)}$$

$$N_g = N_{mandrel}\frac{\cos(\theta_{rc})}{\cos(\theta_{rc})+\left(\alpha\sin(\theta_{gc})-\cos(\theta_{gc})\right)e^{\mu(\theta_{gc}+\theta_{rc}-2\theta_f)}} \quad \text{(Eq. 14a)}$$

$$N_r = N_{mandrel}\left(1-\frac{\cos(\theta_{rc})}{\cos(\theta_{rc})+\left(\alpha\sin(\theta_{gc})-\cos(\theta_{gc})\right)e^{\mu(\theta_{gc}+\theta_{rc}-2\theta_f)}}\right) \quad \text{(Eq. 14b)}$$

Equations 14a and 14b can then be inserted into the piecewise function of Equation 11. As before, the value for θ_f was determined from the finite element model, as were θ_{rc} (=20°), θ_{gc} (=15°) and α (=0.12). The resulting force profile is plotted as the contact correction in Figure 11 (dashed green line). To find the average force in the gauge, the integral of the piecewise function from θ_1 to θ_2 is calculated and then divided by the angle span, as in Equation 2a. This can be reduced to the contact force correction factor found in Equation 15, which is used to produce the final corrected strengths in Table 16.

$$C_{cont} = \frac{(\cos(\theta_{rc})(\cos(\theta_{gc}) - \alpha\, sin(\theta_{gc})))\left(e^{\mu\left(\theta_2+\theta_{gc}-2\theta_f\right)} - 2e^{\mu\left(\theta_{gc}-\theta_f\right)} + e^{\mu(\theta_{gc}-\theta_1)}\right)}{\mu(\theta_2-\theta_1)\left(\cos(\theta_{rc}) + (\alpha\, sin(\theta_{gc}) - \cos(\theta_{gc})\,)e^{\mu\left(\theta_{gc}+\theta_{rc}-2\theta_f\right)}\right)} \quad \text{(Eq. 15)}$$

4. DISCUSSION

The detailed finite element analysis outlined above highlights key differences between the dogbone insert method and the hemicylindrical method of the RTT. As noted in Figure 5, the dogbone load was consistently lower than the hemi load. However, with the corrections for friction and contact, the hemi results are much closer to the input values.

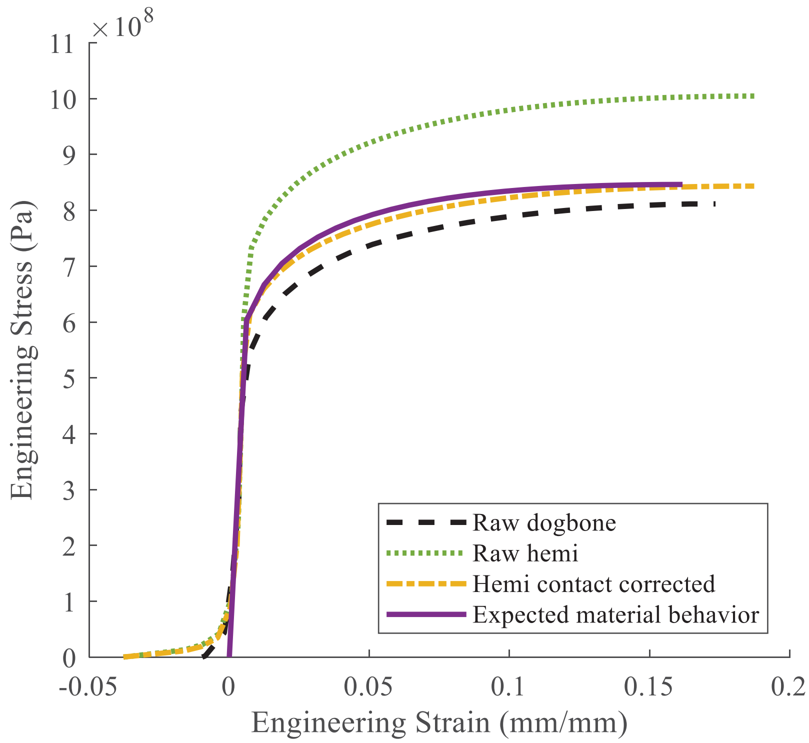

Figure 15 shows the engineering stress vs strain curves for the different methods compared to the material inputs, which is the known behavior of the material. In each case, the apparent strain was adjusted by the difference between the linear elastic region and the expected Young's modulus. This plot visually confirms the findings in Table 16 that the final correction of the hemi data brings the results very close to the expected material behavior. As the finite element results and the expected material behavior are not meant to be accurate past the onset of necking, only data up to UTS is shown.

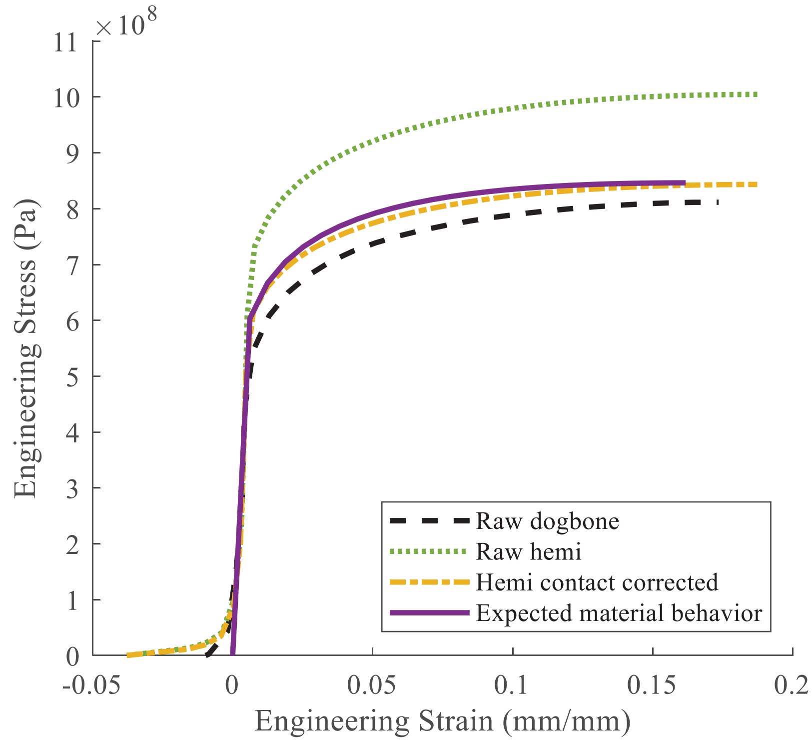

Figure 15: Comparison of Uncorrected dogbone, uncorrected hemi, contact corrected hemi, and the true material inputs. Strain is adjusted to match linear slope with known modulus.

Another noticeable difference between the expected behavior and all the finite element results is the slope in the linear elastic region. Previous research has pointed out that the slope of load-displacement curves generated from RTTs is known to be inaccurate, assuming it is due to slack and compliance in the fixturing, and that it should not be used to measure modulus of elasticity [16]. However, the data generated from this model would not experience any compliance due to fixturing, since the mandrels and dogbone insert are modeled as perfect rigid bodies, and displacement is calculated directly from the relative displacement of the mandrels. Rather, it is likely that the off-normal slope is due in part to deformation of the non-gauged part of the ring. In a conventional tension test, the majority of the test specimen is included in the gauge length, in part to counter this problem [17]. However, in a RTT specimen, the wider non-gauged part of the ring makes up a significant portion of the specimen. Even though the gauge experiences a much higher stress than the rest of the ring (in this case, roughly 5 times higher based on the ratio of widths), the circumference of the ring is much longer than the arc length of the gauge. This can easily be a significant contributor to overall specimen elongation, resulting in a shallower slope in the elastic region. However, the contribution of elastic elongation in the wide part of the ring becomes less significant after yield, as plastic deformation in the gauge portion of the ring begins to dominate the overall elongation comparatively. Another factor that contributes to the shallow slope in the elastic region is the fact that the ring is not undergoing uniaxial stress, uniformly distributed within the gauge. This is apparent especially in the case of the dogbone, which has a shallower slope compared to the hemi. Bending and even premature yielding seen in the dogbone contours of Figure 5 would cause additional, unexpected deformation, and consequently the slope would be even shallower. This is clearly the case for the dogbone curve, as seen in

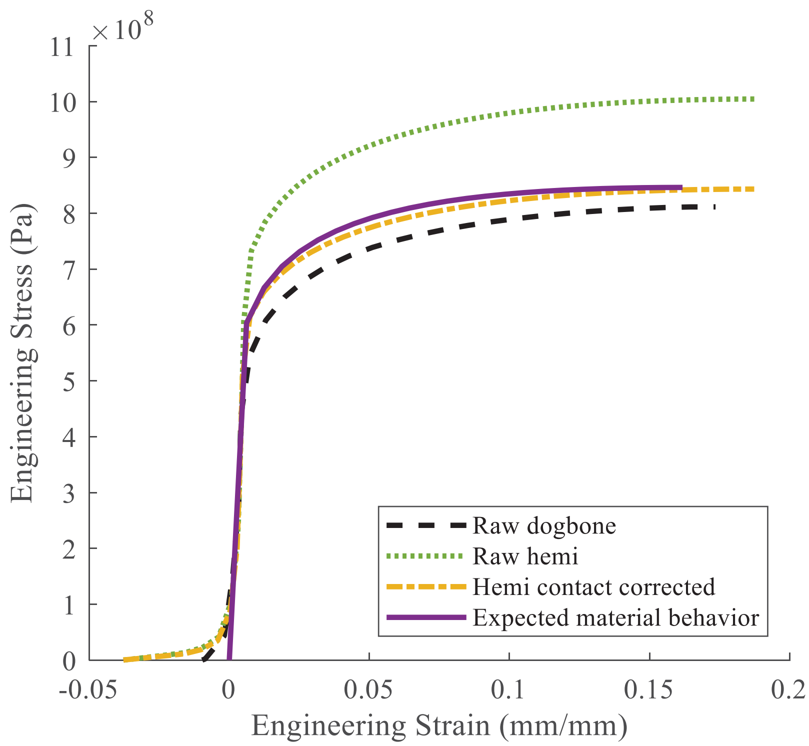

Figure 15.

The hemi method is also shown to be superior to the dogbone method with respect to the parameter variation investigation. The analysis demonstrated the sensitivity of the dogbone method to several parameters, particularly those that impacted the gaps and contact between the mandrels/dogbone insert and the ring. As Arsene and Bai noted in their introduction of this method, care should be taken in determining the geometry that impacts these gaps [23]. However, this analysis showed that even small, uncontrollable variations have a significant effect. While the dimensions of parts such as mandrels and dogbone inserts may be tunable thanks to machining tolerances, other factors will be much more difficult to control experimentally. For instance, the dramatic impact of small changes of inner diameter is noteworthy. Unlike the fixturing, there may be a low degree of control over the dimensions of the tubular material to be tested. This is especially true in the testing of part that have been in service, such as irradiated nuclear fuel cladding. As noted in the introduction, the inner diameter of cladding can change, and other deviations from nominal dimensions such as ovality may occur. These deviations are even more challenging to identify when cladding has been irradiated and must be handled and tested in a hot cell environment. While both the dogbone and the hemi methods showed sensitivity to variations in the design parameters, the dogbone demonstrated a greater degree of sensitivity overall, and for a greater number of parameters, as noted in the results section. Based on this, the hemicylindrical method is likely more desirable in cases where sensitivity is an issue, such as comparing with previous results from different RTT implementations or in challenging environments such as testing in hot cells. When combined with the ability of the hemi to closely match the expected material behavior using suitable mechanics-based correction factors, testing with the hemi method has clear advantages over the dogbone and is recommended as the ideal method for RTT testing.

5. CONCLUSIONS

This work investigated two RTT approaches by using finite element models to replicate experimental setups: one with a dogbone insert supporting the gauge region, and one with a hemicylindrical mandrel supporting the gauge region at a 45° angle. First, the uniformity of stress and strain in the gauge for both methods were investigated, with the hemi method results showing better uniformity. However, both methods either underestimated (the dogbone) or overestimated (the hemi) the YS and UTS compared to the material input. Then, the sensitivity of each method to variation in several parameters was examined. While both showed changes in the load-displacement curves and in the measured strengths, the dogbone method exhibited more sensitivity to a greater number of parameters. Finally, a series of mechanics-based force correction factors for the hemi were considered for their ability to compensate for overestimation of stresses.

With the force correction factor, the measured strengths of the hemicylindrical RTT method closely matched the expected material behavior. The corrected hemi YS and UTS resulted in errors of 0.7% and 0.4% respectively, compared to the dogbone errors of 10.1% and 4.1%. This, combined with the increased sensitivity of the dogbone test method to parameter variation, suggests that the hemicylindrical mandrel approach with a gauge oriented at 45° should be the preferred RTT. Regardless of which approach is used, great care should be taken to understand and measure the precise geometry, as both approaches have shown sensitivity. This is especially important where control of fixture or specimen geometry is challenging, or where comparisons are made with results from other RTT implementations.

5.1 Disclaimer

5.2 Disclosure statement

This manuscript has been authored by Battelle Energy Alliance, LLC under Contract No. DE-AC07-05ID14517 with the U.S. Department of Energy. The United States Government retains and the publisher, by accepting the article for publication, acknowledges that the United States Government retains a nonexclusive, royalty-free, paid-up, irrevocable, world-wide license to publish or reproduce the published form of this manuscript, or allow others to do so, for United States Government purposes.

6. Acknowledgements

This work was funded by the Advanced Fuels Campaign of the U.S. Department of Energy's (DOE) Nuclear Fuel Cycle and Supply Chain (NFCSC) program. This research made use of the resources of the High Performance Computing Center at Idaho National Laboratory, which is supported by the Office of Nuclear Energy of the U.S. Department of Energy and the Nuclear Science User Facilities under Contract No. DE-AC07-05ID14517.

7. References

[1] E. Tenckhoff, *Deformation mechanisms, texture and anisotropy in zirconium and zircaloy*. Germany: Borntraeger, 1980.

[2] J. P. Pragana, I. M. Bragança, C. M. Silva, and P. A. Martins, "Integration of tube end forming in wire arc additive manufacturing: An experimental and numerical investigation," *Int J Adv Manuf Technol*, vol. 117, no. 9, pp. 2715–2726, Dec. 2021, doi: 10.1007/s00170-021-07868-9.

[3] S. J. Zinkle, K. A. Terrani, J. C. Gehin, L. J. Ott, and L. L. Snead, "Accident tolerant fuels for LWRs: A perspective," *Journal of Nuclear Materials*, vol. 448, no. 1, pp. 374–379, May 2014, doi: 10.1016/j.jnucmat.2013.12.005.

[4] J. Desquines, D. A. Koss, A. T. Motta, B. Cazalis, and M. Petit, "The issue of stress state during mechanical tests to assess cladding performance during a reactivity-initiated accident (RIA)," *Journal of Nuclear Materials*, vol. 412, no. 2, pp. 250–267, May 2011, doi: 10.1016/j.jnucmat.2011.03.015.

[5] E. G. Price, "Hydride orientation and tensile properties of Zr-2.5 wt% Nb pressure tubing hydrided while internally pressurized," *Canadian Metallurgical Quarterly*, vol. 11, no. 1, pp. 129–138, Jan. 1972, doi: 10.1179/cmq.1972.11.1.129.

[6] T. ONCHI and H. TANAKA, "Iodine Stress Corrosion Cracking of Unirradiated Zircaloy-2 Tubing by Means of Ring Tension Test," *Journal of Nuclear Science and Technology*, vol. 18, no. 12, pp. 930–939, Dec. 1981, doi: 10.1080/18811248.1981.9733344.

[7] A. V. Shulga, "A comparative study of the mechanical properties and the behavior of carbon and boron in stainless steel cladding tubes fabricated by PM HIP and traditional technologies," *Journal of Nuclear Materials*, vol. 434, no. 1, pp. 133–140, Mar. 2013, doi: 10.1016/j.jnucmat.2012.11.008.

[8] C. P. Dick and Y. P. Korkolis, "Mechanics and full-field deformation study of the Ring Hoop Tension Test," *International Journal of Solids and Structures*, vol. 51, no. 18, pp. 3042–3057, Sep. 2014, doi: 10.1016/j.ijsolstr.2014.04.023.

[9] M. Király, D. M. Antók, L. Horváth, and Z. Hózer, "Evaluation of axial and tangential ultimate tensile strength of zirconium cladding tubes," *Nuclear Engineering and Technology*, vol. 50, no. 3, pp. 425–431, Apr. 2018, doi: 10.1016/j.net.2018.01.002.

[10] M. A. Martín-Rengel, F. J. Gómez Sánchez, J. Ruiz-Hervías, L. Caballero, and A. Valiente, "Revisiting the method to obtain the mechanical properties of hydrided fuel cladding in the hoop direction," *Journal of Nuclear Materials*, vol. 429, no. 1, pp. 276–283, Oct. 2012, doi: 10.1016/j.jnucmat.2012.06.003.

[11] V. Grigoriev, R. Jakobsson, B. Josefsson, and D. Schrire, "Advanced techniques for mechanical testing of irradiated cladding materials," Mar. 2002, Accessed: Nov. 30, 2021. [Online]. Available: https://www.osti.gov/etdeweb/biblio/20246451

[12] S. Arsene and J. Bai, "A new approach to measuring transverse properties of structural tubing by a ring test—experimental investigation," *Journal of Testing and Evaluation*, vol. 26, no. 1, pp. 26–30, 1998.

[13] M. K. Samal, K. S. Balakrishnan, and S. Balakrishnan, "Design Aspects of a Ring Tension Test Setup and Evaluation of Transverse Material Stress-Strain Curve of Tubular Components Using FE Analysis," *Journal of Testing and Evaluation*, vol. 44, no. 6, pp. 2338–2351, 2016.

[14] R. S. Daum *et al.*, "Mechanical property testing of irradiated Zircaloy cladding under reactor transient conditions," in *Small Specimen Test Techniques: Fourth Volume*, ASTM International, 2002.

[15] F. Nindiyasari, P. Pierick, D. Boomstra, and A. Pandit, "Ring tensile test of reference zircaloy cladding tube as a proof of principle for hotcell setup," presented at the TopFuel 2018 Conference, Prague, Czech Republic, 2018.

[16] F. NAGASE, T. SUGIYAMA, and T. FUKETA, "Optimized Ring Tensile Test Method and Hydrogen Effect on Mechanical Properties of Zircaloy Cladding in Hoop Direction," *Journal of*

Nuclear Science and Technology, vol. 46, no. 6, pp. 545–552, Jun. 2009, doi: 10.1080/18811248.2007.9711560.

[17] A. ASTM, “E8/E8M-21, Standard Test Methods for Tension Testing of Metallic Materials. ASTM International, West Conshohocken, 2004.” ASTM International, 2021.

[18] T. M. Link, D. A. Koss, and A. T. Motta, “Failure of Zircaloy cladding under transverse plane-strain deformation,” *Nuclear Engineering and Design*, vol. 186, no. 3, pp. 379–394, Dec. 1998, doi: 10.1016/S0029-5493(98)00284-2.

[19] A. Glendening, D. A. Koss, A. T. Motta, O. N. Pierron, and R. S. Damt, “Failure of hydrided Zircaloy-4 under equal-biaxial and plane-strain tensile deformation,” 2005.

[20] L. A. Yegorova, *Data base on the behavior of high burnup fuel rods with Zr-1% Nb cladding and UO2 fuel (VVER type) under reactivity accident conditions*. Office of Nuclear Regulatory Research, US Nuclear Regulatory Commission, 1999.

[21] J. Kazakeviciute, J. P. Rouse, D. S. A. D. Focatiis, and C. J. Hyde, “The development of a novel technique for small ring specimen tensile testing,” *Theoretical and Applied Fracture Mechanics*, vol. 99, pp. 131–139, 2019, doi: https://doi.org/10.1016/j.tafmec.2018.11.016.

[22] J. Calaf-Chica, J. Martínez-Peña, P. M. B. Díez, and M. P. Calzada, “Ring Hoop Tension Test for yield strength estimation: Numerical analysis for a novel correlation method and applicability for mechanical testing of tubes and pipes,” *Mechanics of Materials*, vol. 169, p. 104295, 2022, doi: https://doi.org/10.1016/j.mechmat.2022.104295.

[23] S. Arsene and J. Bai, “A new approach to measuring transverse properties of structural tubing by a ring test,” *Journal of testing and evaluation*, vol. 24, no. 6, pp. 386–391, 1996.

[24] R. S. Hansen, T. J. Bird, R. Voie, K. Z. Burn, and R. B. Berke, “A high magnification UV lens for high temperature optical strain measurements,” *Review of Scientific Instruments*, vol. 90, no. 4, p. 045117, Apr. 2019, doi: 10.1063/1.5081899.

[25] J. Desquines, B. Cazalis, C. Bernaudat, C. Poussard, X. Averty, and P. Yvon, “Zircaloy-4 fuel cladding mechanical behavior in the field of RIA transients through the PROMETRA program,” 2004.

[26] P. Yvon *et al.*, “Development of new techniques to assess the mechanical behaviour of Zircaloy-4 during an RIA,” *Fuel behaviour under transient and LOCA conditions*, p. 111, 2002.

[27] A. B. Cohen, S. Majumdar, W. E. Ruther, M. C. Billone, H. M. Chung, and L. A. Neimark, “Modified ring stretch tensile testing of Zr-1Nb cladding,” Nuclear Regulatory Commission, Office of Nuclear Regulatory Research, Washington, DC (United States); Brookhaven National Lab. (BNL), Upton, NY (United States), NUREG/CP-0162-Vol.2; CONF-9710101-Vol.2, Mar. 1998. doi: 10.2172/305919.

[28] S.-K. Kim *et al.*, “Hoop strength and ductility evaluation of irradiated fuel cladding,” *Nuclear Engineering and Design*, vol. 239, no. 2, pp. 254–260, Feb. 2009, doi: 10.1016/j.nucengdes.2008.10.024.

[29] L. Jiang, J. J. Jonas, K. Boyle, and P. Martin, “Deformation behavior of two Mg alloys during ring hoop tension testing,” *Materials Science and Engineering: A*, vol. 492, no. 1, pp. 68–73, 2008, doi: https://doi.org/10.1016/j.msea.2008.04.028.

[30] R. Hansen, “High-Magnification Digital Image Correlation Techniques for Aged Nuclear Fuel Cladding Testing,” All Graduate Theses and Dissertations, Utah State University, Logan, Utah, 2021. [Online]. Available: https://digitalcommons.usu.edu/etd/8234

[31] S.-K. Kim, J.-G. Bang, D.-H. Kim, Y.-S. Yang, K.-W. Song, and D.-S. Kim, “Mechanical property evaluation of high burn-up nuclear fuel cladding using the ring tensile test,” *Metals and Materials International*, vol. 15, no. 4, pp. 547–553, 2009.

[32] A. Khalfallah, Z. Ktari, C. Leitão, and J. V. Fernandes, “New Mandrel Design for Ring Hoop Tensile Testing,” *Exp Tech*, vol. 45, no. 6, pp. 769–787, Dec. 2021, doi: 10.1007/s40799-021-00462-4.

[33] H. Wang, R. Bouchard, R. Eagleson, P. Martin, and W. R. Tyson, “Ring hoop tension test (RHTT): A test for transverse tensile properties of tubular materials,” *Journal of Testing and Evaluation*, vol. 30, no. 5, pp. 382–391, 2002.

[34] B.-K. Bae, S.-K. Cho, and C.-S. Seok, “A study on ring tensile specimens,” *Materials Science and Engineering: A*, vol. 483–484, pp. 248–250, Jun. 2008, doi: 10.1016/j.msea.2006.10.203.

[35] D. G. Franklin, “Zircaloy-4 cladding deformation during power reactor irradiation,” in *Zirconium in the Nuclear Industry*, ASTM International, 1982.

[36] F. Qi *et al.*, “Pellet-cladding mechanical interaction analysis of Cr-coated Zircaloy cladding,” *Nuclear Engineering and Design*, vol. 367, p. 110792, Oct. 2020, doi: 10.1016/j.nucengdes.2020.110792.

[37] M. H. A. Piro *et al.*, “2.09 - Pellet-Clad Interaction Behavior in Zirconium Alloy Fuel Cladding☆,” in *Comprehensive Nuclear Materials (Second Edition)*, R. J. M. Konings and R. E. Stoller, Eds. Oxford: Elsevier, 2020, pp. 248–306. doi: 10.1016/B978-0-12-803581-8.09799-X.

[38] V. A. Markelov *et al.*, “Irradiation Test under Advanced PWR Conditions in the Halden Reactor and Post-Irradiation Examination of Fuel Rod Claddings from Different Zirconium Alloys,” presented at the TopFuel 2018 Conference, Prague, Czech Republic, 2018.

[39] R. B. Adamson, C. E. Coleman, and M. Griffiths, “Irradiation creep and growth of zirconium alloys: A critical review,” *Journal of Nuclear Materials*, vol. 521, pp. 167–244, Aug. 2019, doi: 10.1016/j.jnucmat.2019.04.021.

[40] K. M. Paaren, N. Lybeck, K. Mo, P. Medvedev, and D. Porter, “Cladding Profilometry Analysis of Experimental Breeder Reactor-II Metallic Fuel Pins with HT9, D9, and SS316 Cladding,” *Energies*, vol. 14, no. 2, Art. no. 2, Jan. 2021, doi: 10.3390/en14020515.

[41] D. Kamerman *et al.*, “Development of axial and ring hoop tension testing methods for nuclear fuel cladding tubes,” *Nuclear Materials and Energy*, vol. 31, p. 101175, Jun. 2022, doi: 10.1016/j.nme.2022.101175.

[42] K. J. Geelhood, C. E. Beyer, and W. G. Luscher, “PNNL Stress/Strain Correlation for Zircaloy,” Pacific Northwest National Lab. (PNNL), Richland, WA (United States), PNNL-17700, Jul. 2008. doi: 10.2172/969740.